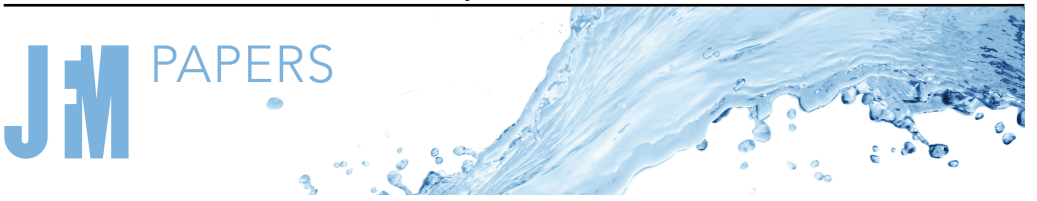
J. Fluid Mech. (2026), *vol.* 1046, A51, doi:10.1017/jfm.2026.12182



The minimal attached eddy in wall turbulence: statistical foundations, inverse identification and influence kernels

Karthik Duraisamy

Department of Aerospace Engineering, University of Michigan, Ann Arbor, MI 48109, USA

Corresponding author: Karthik Duraisamy, kdur@umich.edu

(Received 1 January 2026 UTC; revised 29 August 2026 UTC; accepted 10 September 2026 UTC)

Townsend's attached-eddy hypothesis models the logarithmic region of high-Reynolds-number wall turbulence as a random superposition of wall-attached, self-similar eddies whose sizes obey a scale-invariant population law. Building on the statistical framework of Woodcock & Marusic (2015 *Phys. Fluids*, vol. 27, no. 1, p. 015104), the present work (i) poses an inverse problem to infer the ideal single-eddy contribution (influence) functions for the mean velocity and Reynolds stresses from direct numerical simulations, (ii) uses these inferred kernels to guide a minimal Biot–Savart-consistent hairpin-type eddy built from Rankine vortex rods with an inviscid image system and (iii) introduces and infers a spectral influence kernel that maps a self-similar eddy footprint to its one-dimensional energy spectrum. The influence-kernel viewpoint yields an explanation for the emergence of the linear part of the energy spectrum, provides a clear scale-by-scale decomposition and helps rationalize why simple eddy templates can reproduce a broad set of log-layer statistics once the mean-flow anchoring is fixed. Closed-form expressions for the mean influence function and the Fourier-space streamwise velocity of a general straight-segment hairpin family with image are derived, revealing a mean-variance duality: for a rectangular hairpin, the horizontal head determines the entire mean kernel while the inclined legs dominate the spectral energy. It is shown that the rectangular hairpin yields a precise plateau in the influence function, resulting in a logarithmic mean velocity profile and desirable properties for the streamwise fluctuations. The model is further extended by calibrating the eddy population density as a function of scale, yielding accurate descriptions of mean velocity and streamwise variance across $Re_\tau = 6000-20\,000$.

Key words: turbulent flows, turbulence theory

© The Author(s), 2026. Published by Cambridge University Press.

https://doi.org/10.1017/jfm.2026.12182 Published online by Cambridge University Press

Characterizing and predicting the turbulent flow in the vicinity of a wall continues to not only be a problem of scientific interest, but also one of great practical relevance. Significant knowledge and insight has been gained from the development of experimental diagnostics in the 1960s to the emergence of direct numerical simulations (DNS) in the 1980s, sophisticated measurements in the 1990s, an emphasis on coherent structures in the 2000s and operator-based dynamical models over the past decade. Against this backdrop of increasingly sophisticated experimentation, computations and analyses, the attached-eddy hypothesis – originally proposed more than 50 years ago by Townsend (1976) – continues to serve as a simple, yet effective theory to qualitatively and quantitatively describe structural and statistical aspects of turbulent boundary layers, particularly focusing on the logarithmic region.

The attached-eddy model (AEM) was given a firm mathematical footing by Perry & Chong (1982), and further developed by Marusic and coworkers over the past 25 years (Perry & Marušić 1995; Marusic *et al.* 2013; Woodcock & Marusic 2015; de Silva *et al.* 2016*b*). Among other useful features, the AEM is able to explain scaling behaviours of velocity moments, provide an explanation for uniform momentum zones (de Silva *et al.* 2016*a*) and serve as a predictive model for the von Kármán constant as a function of Reynolds number. A review of the theory and developments of the AEM of wall turbulence can be found in Marusic & Monty (2019). Over the past few years, theoretical and numerical analyses (e.g. McKeon 2019; Lozano-Durán & Bae 2019) have added further credibility to this theory. Despite the success of the AEM, it is pertinent to remember that it is fundamentally a statistical theory, and other hypotheses (e.g. Davidson *et al.* 2006; Davidson & Krogstad 2009) can also be used to explain the statistical characteristics of the log layer.

The attached-eddy hypothesis is based on the principle that the physics and statistical properties of the logarithmic layer can be explained by considering geometrically self-similar eddies that extend from the wall. A foundational assumption is that the length scale of each individual eddy follows a probability distribution that is a function of the distance from the wall. Hence, the term 'attached' alludes to the fact that every eddy can be assumed to be randomly placed on the wall. The AEM is effectively an inviscid theory, yet the range of scales is set by the Reynolds number.

A key advance was made by Woodcock & Marusic (2015) who established a statistical foundation for AEM. They provide a complete derivation for all the velocity moments and demonstrate logarithmic scaling relationships therein. They were also able to provide expressions for the skewness and flatness of the wall-normal and spanwise fluctuations as a function of the Reynolds number. While variants of the AEM continue to be developed in the literature (e.g. Hwang & Eckhardt 2020), we consider Woodcock & Marusic (2015) as the starting point of our exploration and exclusively consider zero pressure gradient boundary layers. The main contributions and guiding questions in this work are as follows.

(i) Inverse identification of attached-eddy influence functions. Townsend introduced the notion of an 'eddy intensity' (or contribution) function: a wall-parallel average of the single-eddy induced velocity and its products. While Townsend gave remarkably insightful descriptions of the nature of this function (figure 5.7, p. 155 of Townsend (1976)), his and most other treatments are qualitative. Here we pose a concrete inverse problem that infers the ideal influence functions $I_1(y/h)$ and $I_{ij}(y/h)$ implied by reference one-point moments (DNS/experiment). The inferred kernels expose the wall-normal support, sign structure and plateau/decay behaviour required for log-layer mean and Reynolds stresses, and motivate a simplified kernel model.

https://doi.org/10.1017/jfm.2026.12182 Published online by Cambridge University Press

(ii) A minimal Biot–Savart-consistent attached eddy. Woodcock & Marusic (2015) utilize an eddy that has a complex shape (figure 1 in Woodcock & Marusic (2015)), presumably configured using insight from DNS and/or particle image velocimetry fields. Guided by the inferred kernels, we construct an attached-eddy template from a small number of Rankine vortex rods (a 'rectangular hairpin') together with an inviscid image system. The objective is not an exact Navier–Stokes solution, but a kinematically consistent building block that (i) respects wall-impermeability, (ii) has well-posed planar influence integrals and (iii) admits a transparent connection between morphology and the influence functions.

(iii) What aspects of morphology control log-layer statistics? We quantify the sensitivity of I_1, I_{ij} and the resulting moments to eddy geometry (e.g. triangular versus square hairpins, inclination angle and simple packet/nesting configurations treated as composite marks). This clarifies which structural features are essential (e.g. realizing the near-constant portion of I_1 for $y/h \lesssim 1$) and which details have weak impact once similarity and attachedness are enforced.

(iv) A spectral influence kernel and interpretation of attached-eddy spectra. We introduce an explicit spectral influence kernel $I_\phi(\kappa_x, \eta)$ that maps a self-similar wall-parallel footprint to its one-dimensional (1-D) streamwise energy spectrum as a function of relative height $\eta = y/h$. Combining I_ϕ with the scale-invariant population law $p(h) \propto h^{-3}$ yields a compact explanation for the emergence (and limitations) of the k_x^{-1} range, the location of the premultiplied hump and the origin of low-k_x discrepancies under the independent-mark (Poisson) hypothesis. The ideal influence kernel is extracted by defining a Fredholm-type inverse problem.

(v) Why the rectangular hairpin is unusually predictive. Exact closed-form expressions for the mean kernel and Fourier-space velocity of a general three-segment hairpin family reveal a clean mean-variance duality: the horizontal head determines the entire mean kernel I_1, while the inclined legs dominate the spectral energy I_ϕ. Within the straight segment family, only the rectangular hairpin produces an exact plateau in I_1 and hence a purely logarithmic mean.

Forward and inverse modelling tools used here are open sourced (https://github.com/CaslabUM/AttachedEddy).

1. Statistics of attached eddies

We begin with a short description of the attached-eddy hypothesis and modelling. This presentation generally follows Woodcock & Marusic (2015) with a slightly different pedagogy. As noted above, we adopt the standard coordinate system: x streamwise, y wall-normal and z spanwise. Planar homogenization/influence integrals are taken over the wall-parallel (x, z) plane, so one-point statistics depend only on y.

Consider a collection of n eddies (figure 1) of length scale $h_{e,i}$ that are placed on the wall at locations $\boldsymbol{x}_{e,i} = (x_{e,i}, z_{e,i})$. Since these are attached eddies, it is implicit that only the streamwise and spanwise components of $\boldsymbol{x}_{e,i}$ are variable. Define $\boldsymbol{h}_e \triangleq \{h_{e,1}, h_{e,2}, .., h_{e,n}\}$ and $\boldsymbol{X}_e \triangleq \{\boldsymbol{x}_{e,1}, \boldsymbol{x}_{e,2}, .., \boldsymbol{x}_{e,n}\}$. Assuming self-similarity and linearity, a quantity q (e.g. a velocity component) evaluated at a location $\boldsymbol{x}$ can be determined using the superposition

$$q(\boldsymbol{x}, \boldsymbol{X}_e, \boldsymbol{h}_e, n) \triangleq \sum_{i=1}^{n} q\left(\frac{\boldsymbol{x} - \boldsymbol{x}_{e,i}}{h_{e,i}}\right). \tag{1.1}$$

https://doi.org/10.1017/jfm.2026.12182 Published online by Cambridge University Press

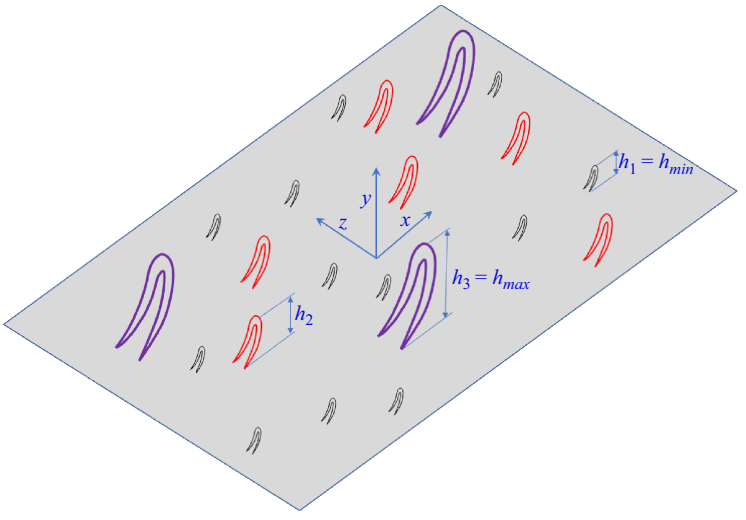


Figure 1. Schematic of discrete representation of attached eddies with $n = 21$ and $m = 3$.

Restricting our attention to a streamwise–spanwise square wall patch of side $2L$ in which the eddies are assumed to be independently and uniformly distributed, and assuming that the range of eddy length scales follows a probability density function $p(h)$, the expectation of q in this region is given by

$$q(\boldsymbol{x}, n) \triangleq \mathbb{E}_{X_e, \boldsymbol{h}_e}\big[q(\boldsymbol{x}, \boldsymbol{X}_e, \boldsymbol{h}_e, n)\big] = \frac{1}{4L^2} \int_{h_{min}}^{h_{max}} \int_{-L}^{L} \int_{-L}^{L} \sum_{i=1}^{n} q\left(\frac{\boldsymbol{x} - \boldsymbol{x}_{e,i}}{h}\right) \, p(h) \, \mathrm{d}x_{e,i} \, \mathrm{d}z_{e,i} \, \mathrm{d}h. \tag{1.2}$$

Homogenizing in the (x, z) directions, and assuming L is large enough that each eddy centred at the origin has a negligible induced contribution outside an area $4L^2$ (cf. Campbell's theorem (Rice 1944) and the appendix of Woodcock & Marusic (2015)), it can be shown that

$$q(y, n) \triangleq \mathbb{E}_{x,z}\big[q(\boldsymbol{x}, n)\big] \approx \frac{n}{4L^2} \int_{h_{min}}^{h_{max}} \int_{-L}^{L} \int_{-L}^{L} q\left(\frac{\boldsymbol{x}}{h}\right) \, p(h) \, \mathrm{d}x \, \mathrm{d}z \, \mathrm{d}h. \tag{1.3}$$

Note that in the above equation, the entire field is written as a function of one prototypical eddy, scaled by the probability density function of the eddy sizes $p(h)$ and the eddy density $n/(4L^2)$. If the mean eddy density is β, then using Poisson's law, the expected value (over all numbers of eddies) is

$$Q(y) \triangleq \mathbb{E}_n\big[q(y, n)\big] = \beta \int_{h_{min}}^{h_{max}} \int_{-L}^{L} \int_{-L}^{L} q\left(\frac{\boldsymbol{x}}{h}\right) \, p(h) \, \mathrm{d}x \, \mathrm{d}z \, \mathrm{d}h. \tag{1.4}$$

Note that all the q defined above are random variables, yet $Q(y)$ is a deterministic quantity. Now we are in a position to define the mean streamwise velocity $U(y)$ as a superposition of eddies of various sizes h. This can be written in terms of the induced velocity field $u_1(\cdot)$

https://doi.org/10.1017/jfm.2026.12182 Published online by Cambridge University Press

of one prototypical eddy,

$$U(y) \triangleq \beta \int_{h_{min}}^{h_{max}} \int_{-L}^{L} \int_{-L}^{L} u_1\left(\frac{\boldsymbol{x}}{h}\right)\ p(h)\,\mathrm{d}x\,\mathrm{d}z\,\mathrm{d}h + U_{ref}$$
$$= \beta \int_{h_{min}}^{h_{max}} p(h)\,h^2\,I_1\left(\frac{y}{h}\right)\,\mathrm{d}h + U_{ref}, \tag{1.5}$$

where the mean-flow eddy contribution (influence) function is

$$I_1\left(\frac{y}{h}\right) \triangleq \int_{-L/h}^{L/h} \int_{-L/h}^{L/h} u_1\left(\frac{\boldsymbol{x}}{h}\right)\ d\left(\frac{x}{h}\right)\ d\left(\frac{z}{h}\right). \tag{1.6}$$

Similarly, we can define the Reynolds stress tensor as

$$R_{ij}(y) \triangleq \beta \int_{h_{min}}^{h_{max}} p(h)\,h^2\,I_{ij}\left(\frac{y}{h}\right)\,\mathrm{d}h,$$
$$\text{where}\quad I_{ij}\left(\frac{y}{h}\right) \triangleq \int_{-L/h}^{L/h} \int_{-L/h}^{L/h} u_i\left(\frac{\boldsymbol{x}}{h}\right)\ u_j\left(\frac{\boldsymbol{x}}{h}\right)\ d\left(\frac{x}{h}\right)\ d\left(\frac{z}{h}\right). \tag{1.7}$$

Note the presence of an additional free stream velocity in the definition of $U(y)$. This is required because we are working with induced velocity fluctuations.

The final piece we need is the probability distribution of the eddy sizes. Using insight from Townsend (1976) and Perry & Chong (1982), Woodcock & Marusic (2015) propose that $p(h) \propto 1/h^3$. In particular, for $h \in [h_{min}, h_{max}]$,

$$p(h) \triangleq \frac{C}{h^3}, \qquad C \triangleq \frac{2}{1/h_{min}^2 - 1/h_{max}^2}. \tag{1.8}$$

Here $h_{max} \approx \delta^+$ is the outer length scale (boundary layer thickness in wall units) and h_{min} is set by the friction Reynolds number in the form $2.6\sqrt{Re_\tau}$.

1.1. *Statistical assumptions and derivation of the Reynolds-stress formula*

The attached-eddy framework above is a shot-noise model: the instantaneous velocity perturbation at a point is written as a superposition of contributions from a random collection of eddies. While the mean follows immediately from linearity of expectation, the Reynolds stresses are quadratic and require an explicit statement of the underlying point-process assumptions.

We idealize the set of attached eddies as a stationary marked Poisson point process Φ on the wall-parallel plane (x, z). Each eddy is characterized by a wall-parallel centre location $\boldsymbol{x}_e = (x_e, z_e)$ and a mark θ that includes its size h (and possibly additional parameters, e.g. orientation, circulation distribution, etc.). The following are assumed:

- Ai. homogeneity – the process is stationary in (x, z) with constant areal intensity β (so the expected number of eddies in area A is βA);
- Aii. independent marking – conditional on the locations, the marks $\{\theta_k\}$ (collectively, all eddy properties beyond the wall-parallel centre location) are independent and identically distributed, and independent of the point locations; in particular the size distribution is $p(h)$;
- Aiii. moment existence – the required single-eddy planar integrals defining I_i and I_{ij} exist in the $L/h \to \infty$ limit (see Appendix A for a convergence discussion);

https://doi.org/10.1017/jfm.2026.12182 Published online by Cambridge University Press

Aiv. ergodic/homogenization interpretation – planar averaging over a sufficiently large patch is identified with the ensemble mean for the stationary process.

Assumptions Ai and Aii are the essential statistical hypotheses behind the Reynolds-stress closure.

Velocity superposition. Let a single prototypical eddy with mark θ induce a velocity field $u_i^{(e)}(\xi, \zeta, \eta; \theta)$ in dimensionless coordinates $(\xi, \zeta, \eta) = (x/h,\ z/h,\ y/h)$. Define the single-eddy planar influence integral

$$I_i(\eta; \theta) \triangleq \int_{\mathbb{R}^2} u_i^{(e)}(\xi, \zeta, \eta; \theta)\, \mathrm{d}\xi\, \mathrm{d}\zeta, \qquad (\eta = y/h). \tag{1.9}$$

Under Ai–Aiii, first-order Campbell/Mecke yields

$$U_i(y) \triangleq \mathbb{E}[u_i(y)] = \beta \int p(h)\, h^2\, \mathbb{E}_{\theta|h}\Big[I_i\Big(\frac{y}{h}; \theta\Big)\Big]\, \mathrm{d}h. \tag{1.10}$$

Second moment and the cross-term issue. The central subtlety is that $u_i u_j = \big(\sum_k u_i^{(k)}\big)\big(\sum_\ell u_j^{(\ell)}\big)$ contains cross terms with $k \neq \ell$, so one cannot in general write the second moment as a sum of 'individual Reynolds stresses'. To make this explicit, expand

$$\mathbb{E}[u_i(y)u_j(y)] = \mathbb{E}\left[\sum_k u_i^{(k)} u_j^{(k)}\right] + \mathbb{E}\left[\sum_{k\neq\ell} u_i^{(k)} u_j^{(\ell)}\right]. \tag{1.11}$$

Define the single-eddy quadratic kernel

$$I_{ij}(\eta; \theta) \triangleq \int_{\mathbb{R}^2} u_i^{(e)}(\xi, \zeta, \eta; \theta)\, u_j^{(e)}(\xi, \zeta, \eta; \theta)\, \mathrm{d}\xi\, \mathrm{d}\zeta. \tag{1.12}$$

For a Poisson process with independent marks (Ai and Aii), the second-order Campbell theorem gives the closed form

$$\mathbb{E}[u_i(y)u_j(y)] = \beta \int p(h)\, h^2\, \mathbb{E}_{\theta|h}\Big[I_{ij}\Big(\frac{y}{h}; \theta\Big)\Big]\, \mathrm{d}h \ + \ U_i(y)\, U_j(y), \tag{1.13}$$

where the $U_i U_j$ term is precisely the contribution of the $k \neq \ell$ cross terms in (1.11). In other words, under Ai and Aii, the cross terms do not vanish individually; rather, they factorize into the product of means.

Reynolds stresses as covariances (cancellation of the cross term). The one-point Reynolds stress tensor is the covariance of the total field:

$$R_{ij}(y) \triangleq \mathbb{E}\big[(u_i(y) - U_i(y))(u_j(y) - U_j(y))\big] = \mathbb{E}[u_i(y)u_j(y)] - U_i(y)U_j(y). \tag{1.14}$$

Substituting (1.13) into (1.14) yields the single-eddy representation

$$R_{ij}(y) = \beta \int p(h)\, h^2\, \mathbb{E}_{\theta|h}\Big[I_{ij}\Big(\frac{y}{h}; \theta\Big)\Big]\, \mathrm{d}h. \tag{1.15}$$

Equation (1.15) is therefore justified only when the eddy field is modelled as a Poisson (or otherwise 'factorizable') superposition with independent marks.

If the eddy process is not Poisson (e.g. clustering, exclusion or explicit packet/nesting correlations), then the cross term in (1.11) no longer factorizes into $U_i U_j$. In that case, (1.13) acquires an additional correction involving the pair (second factorial) moment measure of the process (equivalently a pair-correlation function), and the covariance is no longer determined solely by the single-eddy kernel I_{ij}. A statistically consistent way to incorporate a correlated internal structure (e.g. a hairpin packet) while retaining (1.15) is

https://doi.org/10.1017/jfm.2026.12182 Published online by Cambridge University Press

to treat the packet as the Poisson object: internal correlations are absorbed into the mark θ, while packet centres remain a stationary Poisson field.

1.2. *Convergence of planar influence integrals*

Equation (1.6) defines the mean-flow eddy contribution (influence) function as a planar integral of the streamwise velocity induced by a single prototypical eddy. Writing the dimensionless coordinates $(\xi, \zeta, \eta) \triangleq (x/h,\ z/h,\ y/h)$ and $R \triangleq L/h$, we can make the dependence on the truncation radius explicit,

$$I_1(\eta;\, R) \triangleq \int_{-R}^{R}\int_{-R}^{R} u_1(\xi, \zeta, \eta)\, \mathrm{d}\xi\, \mathrm{d}\zeta, \qquad I_1(\eta) \triangleq \lim_{R\to\infty} I_1(\eta;\, R), \tag{1.16}$$

whenever the limit exists. In particular, we do not assume compact support of the induced velocity field. Rather, the required condition for (1.6) to be well-defined is that the planar integral converges as $R \to \infty$, or equivalently that the tail contribution beyond $|(\xi, \zeta)| \gtrsim R$ becomes negligible for the chosen truncation. A detailed analysis of convergence is presented in Appendix A.

2. The ideal eddy contribution function

The functions $I_1(y/h)$ and $I_{ij}(y/h)$ introduced in (1.6) are key for the moments produced by the attached-eddy model: once these single-eddy planar integrals are specified (together with β and $p(h)$), the attached-eddy integrals yield the one-point mean and Reynolds stresses, and (through similar constructions) higher-order moments. Rather than prescribing a particular eddy geometry *a priori*, we first ask a more direct question:

> Given one-point statistics $U_{data}(y)$ and $R_{ij,data}(y)$ (from DNS or experiment), what shape of $I_1(\eta)$ and $I_{ij}(\eta)$, with $\eta = y/h$, is implied by the attached-eddy integral relations?

This is an inverse problem for a Fredholm integral equation of the first kind. In its continuous form,

$$U_{data}(y) - U_{ref,data} = \beta \int_{h_{min}}^{h_{max}} p(h)\, h^2\, I_1\!\left(\frac{y}{h}\right)\, \mathrm{d}h, \tag{2.1}$$

$$R_{ij,data}(y) = \beta \int_{h_{min}}^{h_{max}} p(h)\, h^2\, I_{ij}\!\left(\frac{y}{h}\right)\, \mathrm{d}h, \tag{2.2}$$

where $U_{ref,data}$ is the outer velocity (e.g. centreline or free stream velocity). For the classical attached-eddy size distribution $p(h) = C/h^3$, these become

$$U_{data}(y) - U_{ref,data} = \beta\, C \int_{h_{min}}^{h_{max}} \frac{I_1(y/h)}{h}\, \mathrm{d}h, \qquad R_{ij,data}(y) = \beta\, C \int_{h_{min}}^{h_{max}} \frac{I_{ij}(y/h)}{h}\, \mathrm{d}h, \tag{2.3}$$

and, after the change of variables $\eta = y/h$ (so that $\mathrm{d}h/h = -\mathrm{d}\eta/\eta$),

$$U_{data}(y) - U_{ref,data} = \beta\, C \int_{y/h_{min}}^{y/h_{max}} \frac{I_1(\eta)}{\eta}\, \mathrm{d}\eta, \qquad R_{ij,data}(y) = \beta\, C \int_{y/h_{max}}^{y/h_{min}} \frac{I_{ij}(\eta)}{\eta}\, \mathrm{d}\eta. \tag{2.4}$$

Equation (2.4) makes two important points transparent: (i) the mapping $I(\eta) \mapsto U(y)$ is smoothing (ill-conditioned to invert without regularization), and (ii) a plateau of $I_1(\eta)$ over $\eta < 1$ immediately yields logarithmic dependence of $U(y)$ on y.

https://doi.org/10.1017/jfm.2026.12182 Published online by Cambridge University Press

2.1. *Discrete formulation and identifiability*

In practice, we discretize the eddy-size range using $\tilde{\boldsymbol{h}} = \{h_1, \ldots, h_m\}$ (log-spaced between h_{min} and h_{max}) and sample the wall-normal coordinate at $\tilde{\boldsymbol{y}} = \{y_1, \ldots, y_{m_y}\}$. The forward map for the mean can be written compactly as

$$\boldsymbol{U}_{data}(\tilde{\boldsymbol{y}}) - U_{ref,data}\mathbf{1} = \boldsymbol{K}(\boldsymbol{c})\boldsymbol{b}, \tag{2.5}$$

where $\boldsymbol{c}$ contains the unknown nodal values of $I_1(\eta)$ (in a chosen basis) and $\boldsymbol{K}$ is the corresponding discretized integral operator (assembled from the weights $p(h)\,h^2$ and the ratios $\eta = y/h$). An analogous system holds for each component I_{ij}.

The discretized velocity moments are

$$\begin{aligned} U_{data}(y_r;\boldsymbol{d}) &= \beta \sum_{l=1}^{m} p(h_l) h_l^2 \left[\sum_q \sum_p u_1\left(\frac{x_p, z_q, y_r}{h_l}; \boldsymbol{d}\right)\left(\frac{\Delta x}{h_l}\right)\left(\frac{\Delta z}{h_l}\right)\right]\Delta h + U_{ref,data} \\ R_{ij,data}(y_r;\boldsymbol{d}) &= \beta \sum_{l=1}^{m} p(h_l) h_l^2 \left[\sum_q \sum_p u_i\left(\frac{x_p, z_q, y_r}{h_l}; \boldsymbol{d}\right) u_j\left(\frac{x_p, z_q, y_r}{h_l}; \boldsymbol{d}\right)\left(\frac{\Delta x}{h_l}\right)\left(\frac{\Delta z}{h_l}\right)\right]\Delta h. \end{aligned} \tag{2.6}$$

Explicitly $K_{ij} = I_1(y_i/h_j)$ and $b_i = \beta p(h_i) h_i^2 \Delta h$. We would now like to extract these coefficients. Towards this end, we define the eddy contribution function at selected locations, and interpolate for the values in other locations in a piecewise linear fashion. In other words

$$\boldsymbol{K} = \begin{bmatrix} I_1(1) & I_1(h_1/h_2) & I_1(h_1/h_3) & .. & I_1(h_1/h_{m-1}) & I_1(h_1/h_m) \\ I_1(h_2/h_1) & I_1(1) & I_1(h_2/h_3) & .. & I_1(h_2/h_{m-1}) & I_1(h_2/h_m) \\ .. & .. & .. & .. & .. & .. \\ I_1(h_m/h_1) & I_1(h_m/h_2) & I_1(h_m/h_3) & .. & I_1(h_m/h_{m-1}) & I_1(1) \end{bmatrix} \tag{2.7}$$

$$\triangleq \begin{bmatrix} c_1 & c_{m+1} & c_{m+2} & .. & c_{2m-2} & c_{2m-1} \\ c_2 & c_1 & c_{m+1} & .. & c_{2m-3} & c_{2m-2} \\ .. & .. & .. & .. & .. & .. \\ c_m & c_{m-1} & c_{m-2} & .. & c_2 & c_1 \end{bmatrix}. \tag{2.8}$$

The unknown $I_1(\cdot)$ values are then interpolated (for instance, if $h_{min} = 186$ and $h_{max} = 5186$ and $m = 11$, then $I_1(h_2/h_3) = 0.42106c_1 + 0.57894c_{12}$) from the nodal locations $\boldsymbol{c}$. Note that there are more unknowns ($2m$) than equations (m), and so while it is possible to determine the unknowns that lead to perfect match of a reference (DNS or experiment) velocity profiles, a choice has to be made on the problem formulation. We choose to solve the following minimum-norm exact interpolation problem:

$$\boldsymbol{c}_{opt} = \min \boldsymbol{c}^T \boldsymbol{c} \;\text{ such that }\; \boldsymbol{U}_{data}(\tilde{\boldsymbol{y}}) - U_{ref,data} = \boldsymbol{K}\boldsymbol{b}. \tag{2.9}$$

Figure 2 shows the optimal eddy contribution functions inferred from the channel flow data (Lee & Moser 2015) at friction Reynolds number $Re_\tau \approx 5200$. Figure 3 confirms that the first and second velocity moments are perfectly reproduced across the entire channel. It is emphasized that the perfect reproduction in figure 3 is expected by construction: the system is underdetermined ($2m$ unknowns, m equations), and the minimum-norm solution exactly satisfies the constraints. The sharp features near $\eta \approx 1$ visible in figure 2 are sensitive to the discretization and the minimum-norm selection criterion; by contrast, the qualitative structure (a near-plateau for $\eta \lesssim 1$ followed by rapid decay) is robust

https://doi.org/10.1017/jfm.2026.12182 Published online by Cambridge University Press

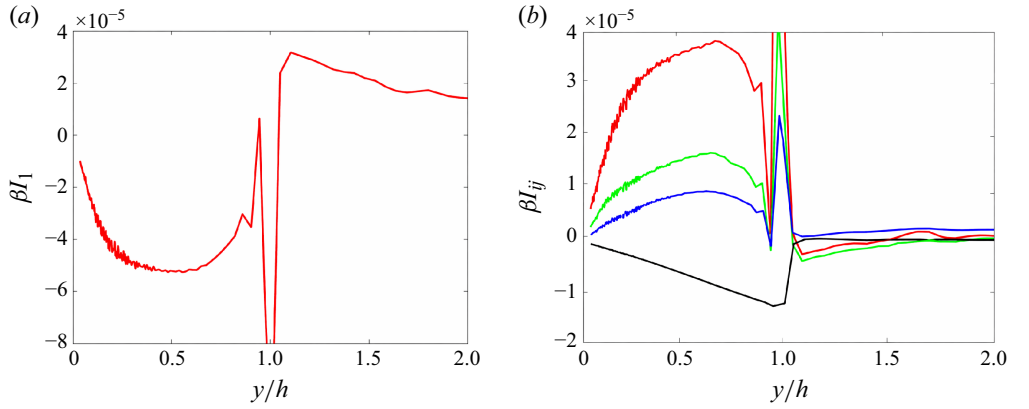


Figure 2. Optimal influence functions for $Re_\tau \approx 5200$ for the mean flow (a) and Reynolds stresses (b). Here red , streamwise; green spanwise; blue wall-normal and black , shear).

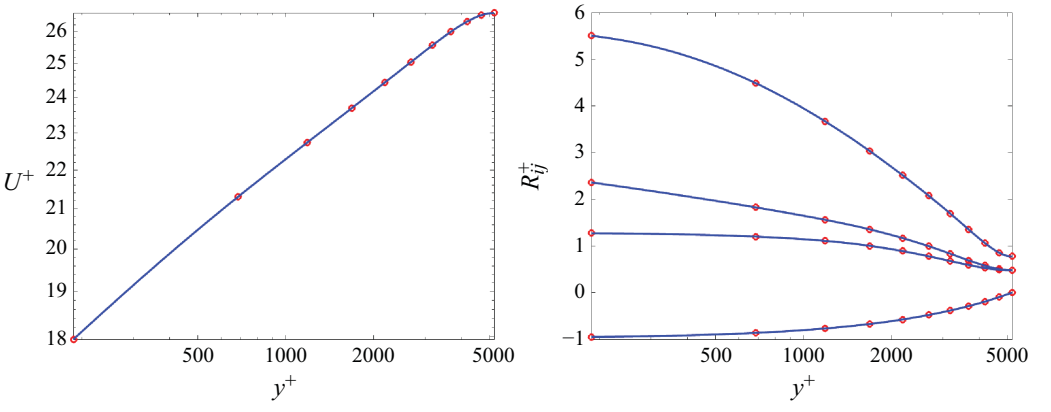


Figure 3. Reference (symbols) versus optimal attached-eddy statistics for $Re_\tau \approx 5200$. The moments are reconstructed from the inferred I_1 and I_{ij} via (1.5) and (1.15). The lowest y^+ shown corresponds approximately to h_{min}, below which the AEM has no eddies and the model is not expected to apply.

across different discretizations, regularization strategies and data sources. It is this robust qualitative structure, rather than the fine details, that motivates the simplified model in § 2.2. The inversion uses moments across the full channel half-height (y^+ from h_{min} to h_{max}), so the inferred $I_1(\eta)$ and $I_{ij}(\eta)$ are constrained by the entire wall-normal profile, not only the log layer.

2.2. *A simplified influence-function model and the log law*

We remark that the underlying physics is more complex than attached eddies can represent. The inverse problem, however, yields a function that, while smooth, has a visually interpretable structure: a near-plateau over $\eta = y/h \lesssim 1$ followed by a transition and decay for $\eta > 1$. This motivates the simple piecewise model shown in figure 4.

Consider a collection of attached eddies that result in a simple function as shown in figure 4. It will be shown below that it is indeed possible to construct an attached eddy that corresponds to such a function. Using this influence function, one can reconstruct the

https://doi.org/10.1017/jfm.2026.12182 Published online by Cambridge University Press

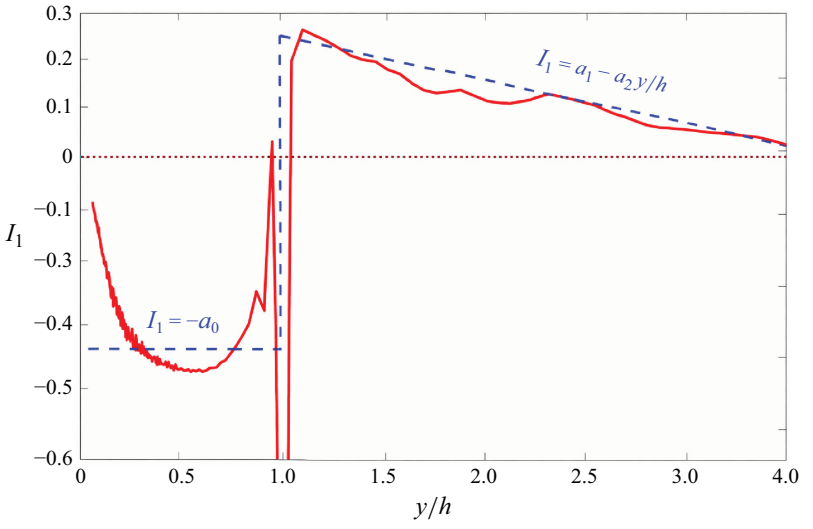


Figure 4. A hypothetical model of the eddy influence function corresponding to the mean streamwise velocity (blue dashed lines) compared with the optimal influence function.

mean streamwise velocity as

$$\begin{aligned} U(y) &= \frac{2\beta}{1/h_{min}^2 - 1/h_{max}^2} \int_{h_{min}}^{h_{max}} \frac{I_1\,(y/h)}{h} \mathrm{d}h + U_{ref} \\ &\approx \frac{2\beta}{1/h_{min}^2 - 1/h_{max}^2} \left[\int_{y/h_{max}}^{1} \frac{-a_0}{y/h} d(y/h) + \int_{1}^{a_1/a_2} \frac{a_1 - a_2 y/h}{y/h} d(y/h) \right] + U_{ref} \\ &= \frac{2\beta}{1/h_{min}^2 - 1/h_{max}^2} \left[a_0 \log[y/h_{max}] + a_1 \log[a_1/a_2] - a_1 + a_2 \right] + U_{ref}. \end{aligned} \tag{2.10}$$

It is thus clear that the von Kármán constant can be constructed as

$$\kappa = \frac{1/h_{min}^2 - 1/h_{max}^2}{2a_0\beta}. \tag{2.11}$$

Note that Woodcock & Marusic (2015) use a Taylor series approximation on a generic eddy to derive an alternate expression for κ. While that is insightful, it is perhaps a valid approximation only for certain types of eddy influence functions.

Equation (2.11) provides a direct route from measurable quantities (κ, Re_τ) and the eddy population density β to the plateau value a_0 of the influence function, or conversely, from the inferred a_0 and a prescribed β to a prediction of κ. As will be shown in the following sections, employing a rectangular hairpin yields a precisely constant I_1 for $y/h \leq 1$. In §§ 3 and 4, β is chosen to fit the log law slope. In § 6, a variable β model is prescribed.

3. Predictive model and insights

Now, we answer the question whether it is possible to recreate the above hypothetical influence function using an attached eddy. Consider a hairpin (figure 5) with unit circulation as the attached eddy, along with its image across the $y = 0$ plane to enforce no-penetration. We consistently achieved good results using Rankine vortex rods instead

https://doi.org/10.1017/jfm.2026.12182 Published online by Cambridge University Press

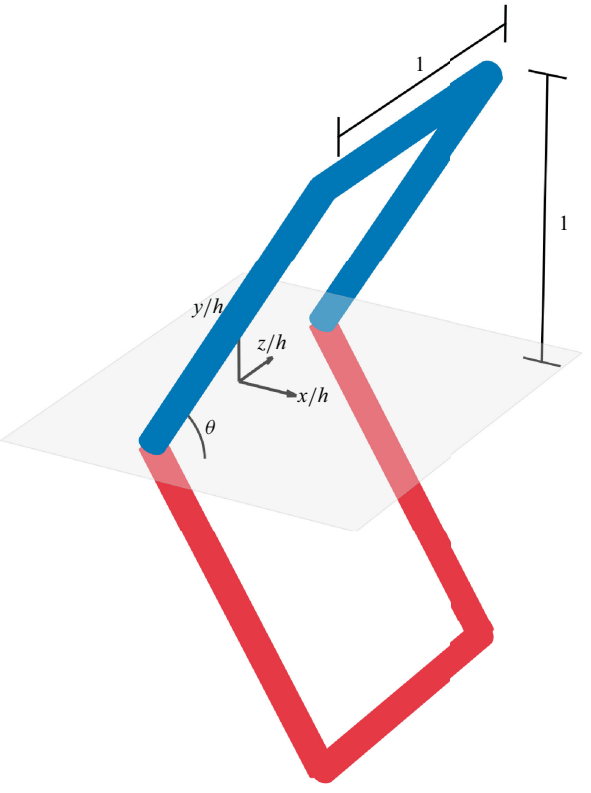


Figure 5. A prototypical hairpin-type eddy.

of vortex filaments. All the results henceforth correspond to vortex segments represented as Rankine vortex rods with core radius ≈ 0.025 units relative to figure 5.

It is remarked that this eddy corresponds to a closed loop in the sense that the leg of the eddy aligned with the wall is cancelled by an equal and opposite image vortex pair, and is thus consistent with the vorticity kinematics. Using the Biot–Savart law to compute the induced velocity u_1 in (1.6), figure 6 shows that such a simple attached eddy can reproduce the mean streamwise velocity accurately. Further, the second moments are shown in figure 6, and the Reynolds stresses trends are well-predicted, though the spanwise stresses are over-estimated in the region $y^+ < 2000$.

It is noted that an extensive optimization was performed on different eddy shapes (e.g. triangular hairpin) and packet configurations. Yet, these did not yield improved predictions, particularly encountering difficulties in matching the log law slope while providing reasonable second moment and spectral behaviour. The reasons behind this observation will be examined in detail in § 5.

The rectangular hairpin at an angle of $\theta = 60°$ is close to the optimal solution across different metrics and shows comparisons with the experimental measurements from Samie *et al.* (2018). As shown in figures 7, 8 and 9, the model remains remarkably accurate in predicting mean velocity, streamwise Reynolds stress and spectra over a range of Reynolds numbers.

We note that the influence functions were inferred from channel flow DNS at $Re_\tau \approx 5200$ (Lee & Moser 2015), whereas the predictions in figures 7, 8 and 9 are

https://doi.org/10.1017/jfm.2026.12182 Published online by Cambridge University Press

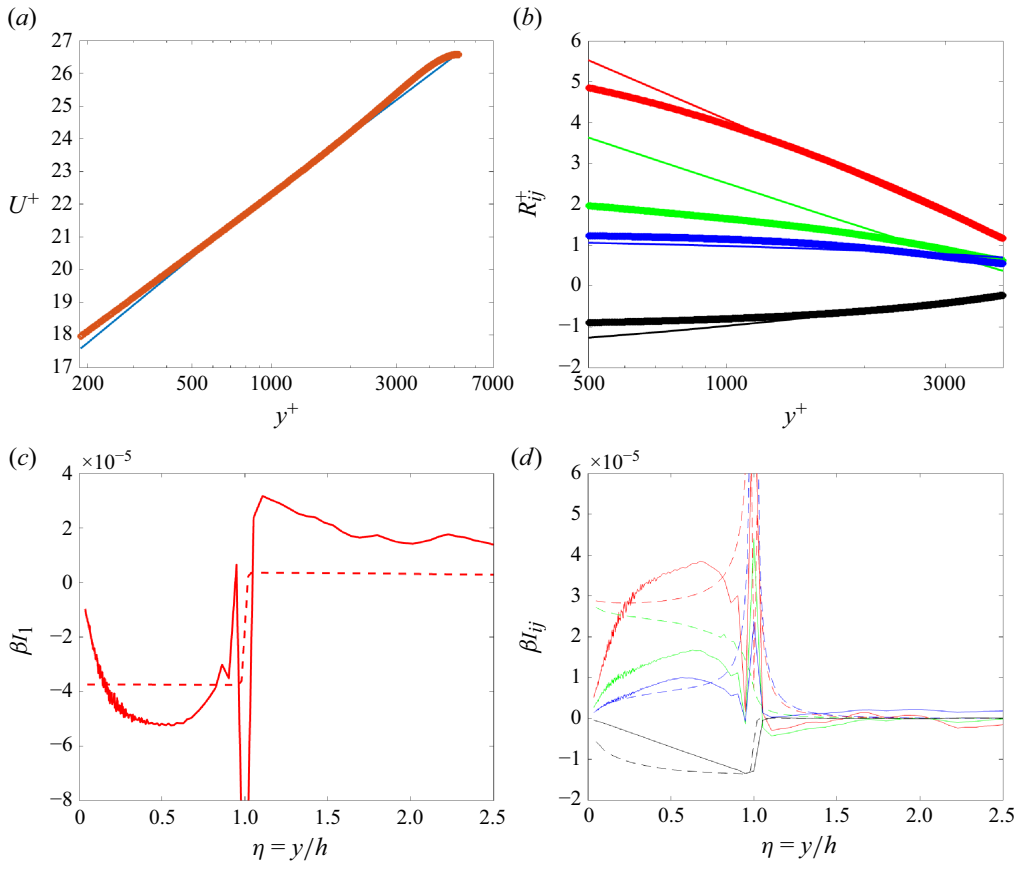


Figure 6. Panels (*a*) and (*b*) show velocity moments: symbols, data; lines, rectangular hairpin at $\theta = 60°$. Panels (*c*) and (*d*) show eddy influence functions: solid lines, optimal eddy influence function; dashed lines, rectangular hairpin at $\theta = 60°$. For (*a*) and (*c*), colours follow figure 2. Note that the $y^+ < 500$ region is not shown here because in the second moments, the log scaling takes hold in the outer part of the log layer. Refer figure 19 for a full view of this phenomenon.

compared with zero-pressure-gradient boundary layer measurements at $Re_\tau = 6000$–$20\,000$ (Samie *et al.* 2018). The fact that the same eddy template transfers successfully across flow geometries supports the universality of the log-layer structure, but this correspondence deserves further scrutiny, particularly for the Reynolds stress components and for the outer region where channel and boundary layer statistics diverge.

We also note that the model predictions align better with the data above the log layer than within it. This is not contradictory despite $p(h) \propto h^{-3}$ being questionable in the outer region: the rapid decay of $I_1(\eta)$ for $\eta > 1$ ensures that the outer-region statistics are dominated by the largest eddies ($h \sim h_{max}$), whose population amplitude is anchored by β through the log-law calibration. The kernel structure naturally suppresses contributions from eddies smaller than the observation height, so the model works above the log layer primarily because of the influence-function shape rather than the population law.

The inverse problem strongly constrains what any viable attached eddy must do in a wall-parallel plane. In particular, the inferred mean influence function $I_1(y/h)$ exhibits (*a*) a near-constant region for $y/h \lesssim 1$ and (*b*) rapid decay for $y/h \gtrsim 1$, implying that eddies larger than the observation height dominate the log-region population integral.

https://doi.org/10.1017/jfm.2026.12182 Published online by Cambridge University Press

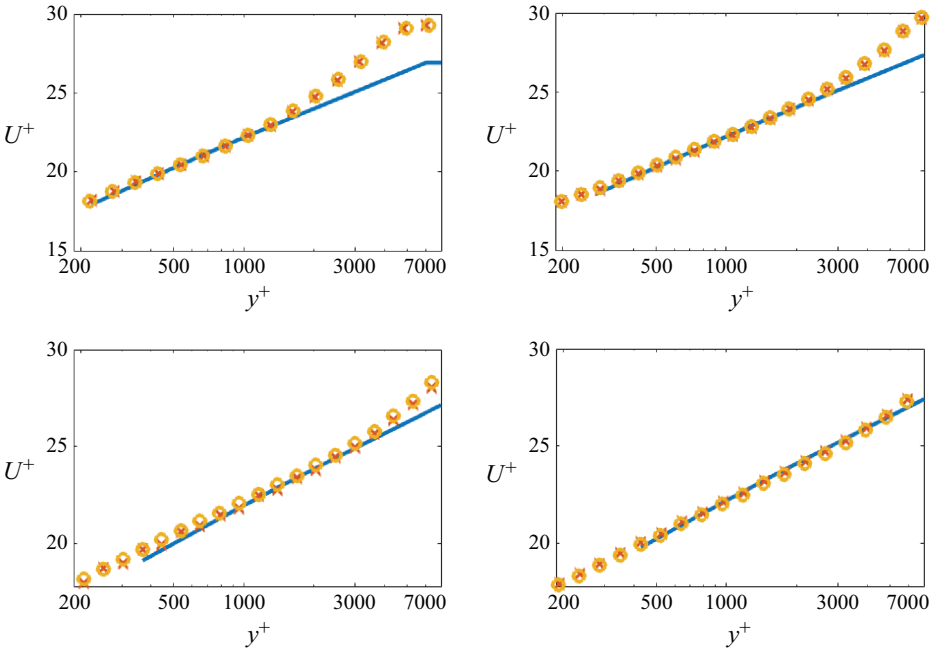


Figure 7. Mean velocity prediction using rectangular hairpin at $\theta = 60°$ for $Re_\tau = [6000, 10\,000, 14\,500, 20\,000]$. Symbols: Samie *et al.* (2018).

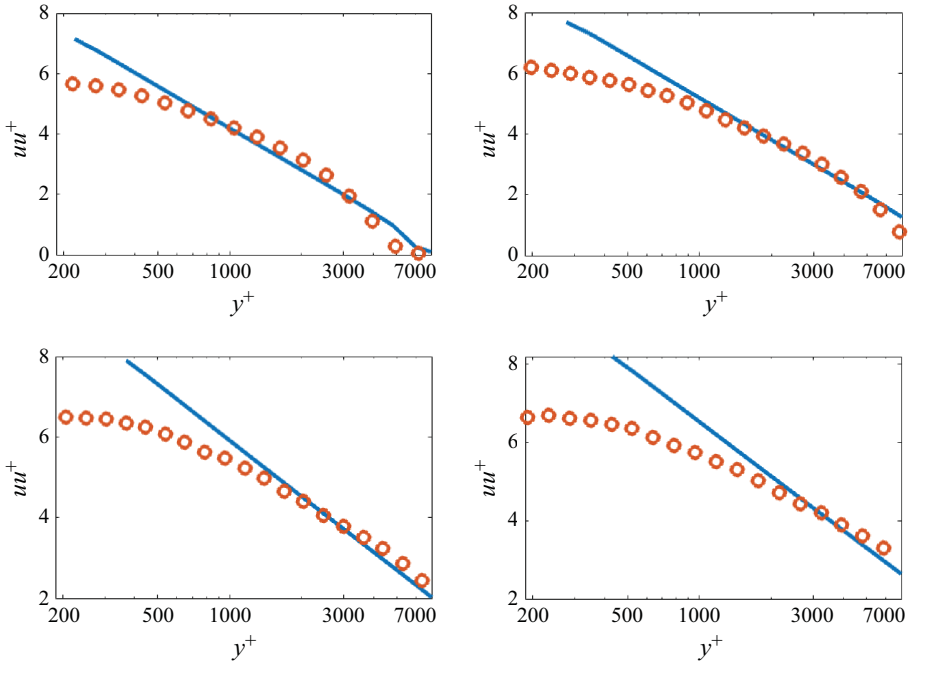


Figure 8. Streamwise velocity fluctuation predictions using rectangular hairpin at $\theta = 60°$ for $Re_\tau = [6000, 10\,000, 14\,500, 20\,000]$. Symbols: Samie *et al.* (2018).

https://doi.org/10.1017/jfm.2026.12182 Published online by Cambridge University Press

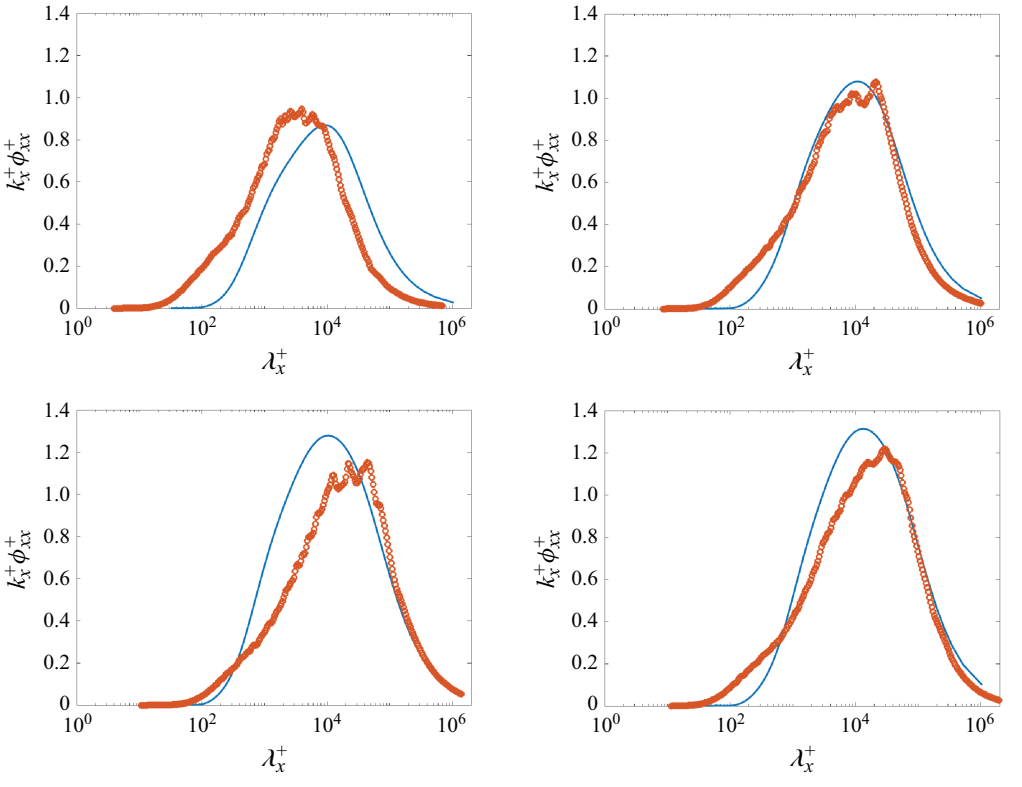


Figure 9. Premultiplied streamwise energy spectra predictions at $y^+ = 1184$ using rectangular hairpin at $\theta = 60°$ for $Re_\tau = [6000, 10\,000, 14\,500, 20\,000]$. Symbols: Samie *et al.* (2018).

The rectangular hairpin + image realizes these features because the two legs and head generate partially cancelling far-field contributions, while the inviscid image enforces wall compatibility and suppresses the leading-order tail that would otherwise make the planar influence integrals marginal (Appendix A). By contrast, a triangular hairpin produces a more monotone 'ramp' in I_1 and does not reproduce the inferred plateau as cleanly (figure 6). Experimentation with a pack of triangular hairpins with variable circulation strengths did not improve results beyond the rectangular hairpin which appears optimal.

The inclined hairpin footprint produces elongated streamwise u signatures, which is precisely the kind of wall-parallel signature that feeds the low-k_x premultiplied hump. The log-layer statistics depend weakly on microscopic details once a few structural constraints are met. This eddy structure appears to have some key features that yield accurate streamwise energy spectra in the log layer. We examine this below by providing an explicit similarity map from eddy morphology to the single-eddy spectrum as a function of relative height.

4. The influence kernel

The planar influence functions $I_1(y/h)$ and $I_{ij}(y/h)$ govern one-point moments via (1.5) and (1.15). For spectra, we introduce an analogous spectral influence kernel $I_\phi(\kappa_x, \eta)$ that compactly summarizes how a single self-similar eddy distributes streamwise energy across wavenumbers as a function of relative height $\eta = y/h$. To the author's knowledge, making this kernel explicit is not common in the attached-eddy literature; it is useful because it

https://doi.org/10.1017/jfm.2026.12182 Published online by Cambridge University Press

cleanly separates single-eddy geometry (captured by I_ϕ) from population effects (captured by $p(h)$ and β).

Under our geometric and circulation scaling assumptions, the hairpin footprint is self-similar,

$$\mathcal{U}\Big(\frac{x}{h}, \frac{z}{h}, \frac{y}{h}\Big) = \mathcal{U}(\xi, \zeta, \eta), \tag{4.1}$$

where $\mathcal{U}$ is the unit-eddy footprint expressed in dimensionless coordinates. Taking the Fourier transform and changing variables yields the exact scaling $\widehat{u}_h(k_x, k_z; y) \triangleq h^2\, \widehat{\mathcal{U}}(\kappa_x, \kappa_z; \eta)$, where $\widehat{\mathcal{U}}(\kappa_x, \kappa_z; \eta) \triangleq \int_{\mathbb{R}^2} \mathcal{U}(\xi, \zeta, \eta)\, e^{-i(\kappa_x \xi + \kappa_z \zeta)}\, \mathrm{d}\xi\, \mathrm{d}\zeta$. Therefore

$$\Phi_{xx}^{(h)}(k_x, k_z; y) = \frac{h^4}{(2\pi)^2}\, \big|\widehat{\mathcal{U}}(\kappa_x, \kappa_z; \eta)\big|^2 . \tag{4.2}$$

Integrating over k_z and using $k_z = \kappa_z / h$ gives the scalewise spectrum

$$\phi_{xx}^{(h)}(k_x; y) \triangleq \int_{-\infty}^{\infty} \Phi_{xx}^{(h)}(k_x, k_z; y)\, \mathrm{d}k_z = h^3\, I_\phi(\kappa_x, \eta), \tag{4.3}$$

where we define the influence kernel as

$$I_\phi(\kappa_x, \eta) \triangleq \frac{1}{(2\pi)^2} \int_{-\infty}^{\infty} \big|\widehat{\mathcal{U}}(\kappa_x, \kappa_z; \eta)\big|^2\, \mathrm{d}\kappa_z. \tag{4.4}$$

This identity is a concrete mathematical object that will help decode the energy spectrum in greater detail. In the following subsection, we will formulate an inverse problem to extract the shape of the ideal kernel.

It is noted that the spectral influence kernel is related to the one-point Reynolds stress kernel by $I_{11}(\eta) = \int_0^\infty I_\phi(\kappa_x, \eta)\, \mathrm{d}\kappa_x$, providing a consistency check between the spectral and one-point inverse problems.

4.1. *Inverse problem to extract ideal influence kernel*

The inversion uses the attached-eddy spectral superposition in the form

$$\phi_{xx}(k_x; y) = \int_{h_{min}}^{h_{max}} \psi(k_x h, y/h)\, \mathrm{d}h, \tag{4.5}$$

where

$$\psi(\kappa, \eta) = \beta C\, I_\phi(\kappa_x, \eta), \qquad \kappa_x = k_x h, \qquad \eta = y/h. \tag{4.6}$$

The numerical inversion solves for a gridded approximation to ψ. The kernel is represented on a tensor-product grid in (κ, η), and the unknown vector is the row-major flattening of the $n_\eta \times n_\kappa$ kernel array,

$$\boldsymbol{x} = \mathrm{vec}(\Psi) \in \mathbb{R}^{n_\eta n_\kappa}, \qquad \Psi_{b,a} \approx \psi(\kappa_a, \eta_b), \tag{4.7}$$

with the index map $\ell(b, a) = (b-1)n_\kappa + a, \quad 1 \le a \le n_\kappa, \quad 1 \le b \le n_\eta$. Hence $\boldsymbol{x} = [\Psi_{1,1}, \Psi_{1,2}, \ldots, \Psi_{1,n_\kappa}, \Psi_{2,1}, \ldots, \Psi_{n_\eta,n_\kappa}]^T$. Equation (4.5) is integrated over h using n_h geometrically spaced nodes $h_1, \ldots, h_{n_h} \in [h_{min}, h_{max}]$. The quadrature weights for a finite difference approximation are

$$\begin{aligned} w_1 &= h_2 - h_1, \\ w_q &= \frac{1}{2}(h_{q+1} - h_{q-1}), \qquad 2 \le q \le n_h - 1, \\ w_{n_h} &= h_{n_h} - h_{n_h - 1}. \end{aligned} \tag{4.8}$$

https://doi.org/10.1017/jfm.2026.12182 Published online by Cambridge University Press

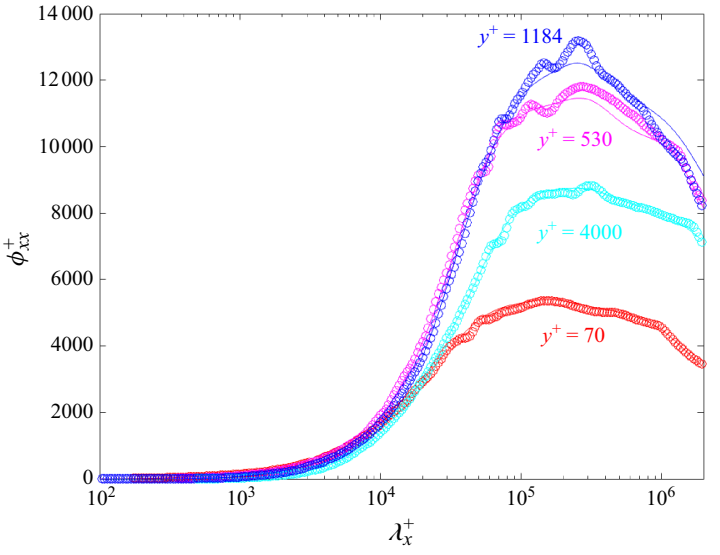


Figure 10. Data (symbols) and reconstructed (lines) streamwise energy spectra $\phi^+_{xx}(\kappa_x)$ for a few wall normal locations.

We then solve the non-negative regularized least-squares problem

$$\min_{\boldsymbol{x}\geq 0} \frac{1}{2}\|\boldsymbol{A}\boldsymbol{x}-\boldsymbol{b}\|_2^2 + \frac{\lambda_\kappa^2}{2}\|\boldsymbol{L}_\kappa \boldsymbol{x}\|_2^2 + \frac{\lambda_\eta^2}{2}\|\boldsymbol{L}_\eta \boldsymbol{x}\|_2^2 + \frac{\lambda_0^2}{2}\|\boldsymbol{L}_0 \boldsymbol{x}\|_2^2. \tag{4.9}$$

Equivalently, this is written as an augmented non-negative least-squares problem

$$\min_{\boldsymbol{x}\geq 0} \frac{1}{2}\|\widetilde{\boldsymbol{A}}\boldsymbol{x}-\widetilde{\boldsymbol{b}}\|_2^2, \tag{4.10}$$

with

$$\widetilde{\boldsymbol{A}} = \begin{bmatrix} \boldsymbol{A} \\ \lambda_\kappa \boldsymbol{L}_\kappa \\ \lambda_\eta \boldsymbol{L}_\eta \\ \lambda_0 \boldsymbol{L}_0 \end{bmatrix}, \qquad \widetilde{\boldsymbol{b}} = \begin{bmatrix} \boldsymbol{b} \\ \boldsymbol{0} \\ \boldsymbol{0} \\ \boldsymbol{0} \end{bmatrix}. \tag{4.11}$$

For the reported results, $\widetilde{\boldsymbol{A}} \in \mathbb{R}^{28159\times 5712}$, $\text{nnz}(\widetilde{\boldsymbol{A}}) = 1029731$ and $\lambda_\kappa = 10^{-1}$, $\lambda_\eta = 4\times 10^{-1}$, $\lambda_0 = 10^{-5}$. While these numbers appear arbitrary, the goal is to obtain insight into the shape of the kernel, and thus the primary metric is to obtain a smooth solution that does not overfit to measurement noise.

Appendix B provides more detail on the construction of these matrices. This is a more complicated inverse problem than the ones introduced earlier. Equation (4.10) is solved by projected FISTA (Buccini *et al.* 2025). Figure 10 shows the reconstructed streamwise energy spectra (from the inverse solution) and how it compares with the data. The agreement is good, and regularization is shown to smooth the solution to a small degree, but not enough to impact any conclusions.

The spectral data used for this inversion are from the experimental measurements of Samie *et al.* (2018) at $Re_\tau = 20\,000$. A brief sensitivity study on the regularization weights $(\lambda_\kappa, \lambda_\eta, \lambda_0)$ confirmed that the qualitative shape of I_ϕ, in particular the broad plateau at

https://doi.org/10.1017/jfm.2026.12182 Published online by Cambridge University Press

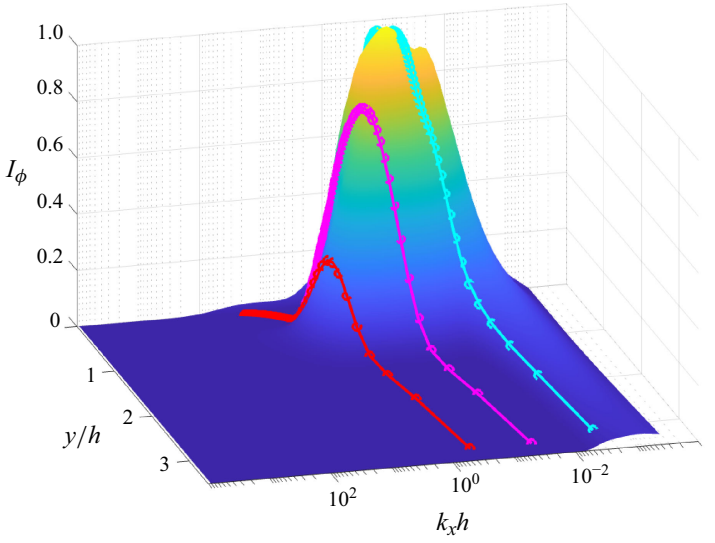


Figure 11. Inferred streamwise energy influence kernel $I_\phi(\kappa_x, \eta)$ (normalized peak value). This figure highlights that the kernel has a broad, elevated region at small η and small-to-moderate κ, and a more localized hump as η increases. Also shown are contributions to $\phi^+_{xx}(k^+_x)$ for $k^+_x = 1 \times 10^{-5}$ (cyan) and $k^+_x = 1 \times 10^{-4}$ (magenta) and $k^+_x = 1 \times 10^{-3}$ (red) at $y^+ = 1184$ for $Re_\tau = 20\,000$.

small η and the localized hump at $\eta \sim O(1)$ is robust though finer features of the kernel near $\kappa_x \to 0$ are sensitive to the choice of λ_κ.

The extracted kernel $I_\phi(\kappa_x, \eta)$, which is a function of the dimensionless wavenumber $\kappa_x = k_x h$ at fixed relative height $\eta = y/h$ and is shown in figure 11. It is immediately clear that eddies of scale $h < y$ have negligible influence on the statistics.

For any fixed η, typical scaling arguments yield a concentration of the influence $I_\phi(\kappa_x, \eta)$ around $\kappa_x = O(1)$ because κ_x is the only dimensionless streamwise wavenumber available to the unit eddy. Therefore, for a given size h and fixed y, the dominant contribution of that eddy appears around

$$k_x h = O(1) \quad \Longleftrightarrow \quad k_x = O(1/h), \tag{4.12}$$

equivalently $\lambda_x = 2\pi/k_x = O(h)$. This explains the peak of the premultiplied spectra in figure 9.

The rectangular hairpin AEM is able to recover a near-perfect linear behaviour of the streamwise energy spectrum in the intermediate scale range as shown in figure 12. Below, we will give more concrete and quantitative explanations.

4.2. *From single-eddy spectra to the attached-eddy spectrum*

The attached-eddy prediction for the 1-D spectrum is the population superposition

$$\phi_{xx}(k_x; y) = \beta \int_{h_{min}}^{h_{max}} p(h)\, \phi^{(h)}_{xx}(k_x; y)\, \mathrm{d}h, \qquad p(h) = \frac{C}{h^3}. \tag{4.13}$$

Insert the exact single-eddy factorization:

$$\phi_{xx}(k_x; y) = \beta \int_{h_{min}}^{h_{max}} \frac{C}{h^3} \left(h^3\, I_\phi(k_x h, y/h) \right) \mathrm{d}h = \beta\, C \int_{h_{min}}^{h_{max}} I_\phi(k_x h, y/h)\, \mathrm{d}h. \tag{4.14}$$

https://doi.org/10.1017/jfm.2026.12182 Published online by Cambridge University Press

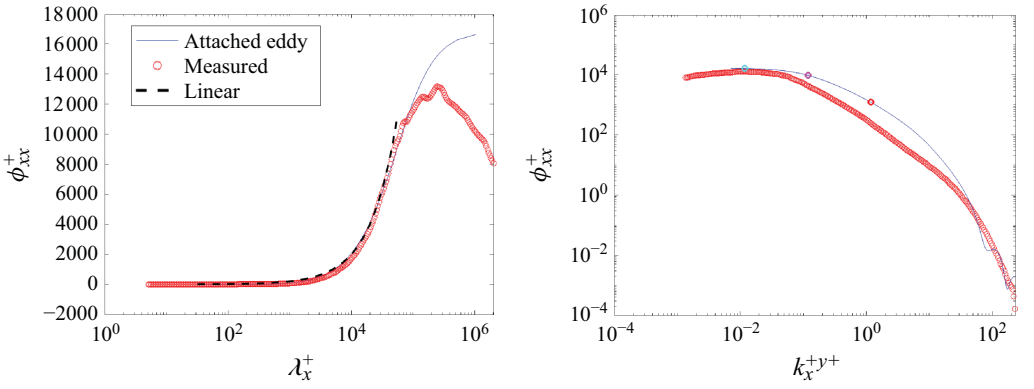


Figure 12. Streamwise energy spectra at $y^+ = 1184$ for $Re_\tau = 20\,000$.

Change variables $\kappa = k_x h$ so $\mathrm{d}h = \mathrm{d}\kappa/k_x$, and note that $y/h = yk_x/\kappa$:

$$\phi_{xx}(k_x;\, y) = \frac{\beta\, C}{k_x} \int_{k_x h_{min}}^{k_x h_{max}} I_\phi\left(\kappa,\, \frac{yk_x}{\kappa}\right) \mathrm{d}\kappa. \tag{4.15}$$

Define the integral factor

$$F(k_x;\, y) = \int_{k_x h_{min}}^{k_x h_{max}} I_\phi\left(\kappa,\, \frac{yk_x}{\kappa}\right) \mathrm{d}\kappa, \tag{4.16}$$

so that

$$\phi_{xx}(k_x;\, y) = \frac{\beta\, C}{k_x}\, F(k_x;\, y). \tag{4.17}$$

The $1/k_x$ scaling in the logarithmic region arises when $F(k_x;\, y)$ varies slowly with k_x over an intermediate band. This occurs when the κ-window $[k_x h_{min},\, k_x h_{max}]$ covers the portion of the kernel $I_\phi(\kappa,\, \eta)$ that carries most of the contribution, and when the effective η values encountered (through $\eta = y/h = yk_x/\kappa$) lie in the log-layer-relevant range. In that band,

$$F(k_x;\, y) \approx \text{constant} \quad \Longrightarrow \quad \phi_{xx}(k_x;\, y) \propto \frac{1}{k_x} \propto \lambda_x. \tag{4.18}$$

This is substantiated by the results in figure 13.

The above '$1/k_x$' argument corresponds to the case that $F(k_x;\, y)$ is approximately constant over an intermediate k_x range. However, the low-k_x behaviour is entirely controlled by how $F(k_x;\, y)$ varies as $k_x \to 0$. There is no universality guarantee there: when k_x is small, the κ-window and the η-trajectory can force the integral to sample the least robust part of the kernel.

This is visible in the kernel visualization. Figure 11 shows the kernel surface, and figure 13 shows three trajectories corresponding to fixed k_x^+ values. The low-κ region of the kernel is where $I_\phi(\kappa,\, \eta)$ typically changes most rapidly. In such a regime, the integral $F(k_x;\, y)$ cannot be expected to be constant: small shifts in k_x move both the integration bounds and the trajectory through $(\kappa,\, \eta)$, producing non-negligible changes in F.

The overprediction of streamwise energy spectra by the AEM in the high wavelength limit is clearly explained by figures 14 and 15. For small κ_x, this trajectory spends substantial 'arclength' in the region of small κ and small η and I_ϕ does not reduce to zero for small κ_x as in figure 11. Nevertheless, the overall shape of the kernel and the

https://doi.org/10.1017/jfm.2026.12182 Published online by Cambridge University Press

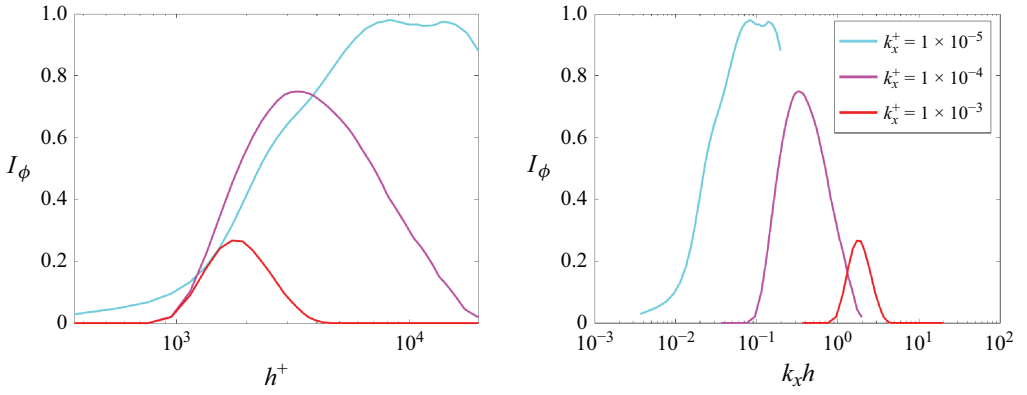


Figure 13. Contribution to F integral from different scales at $y^+ = 1184$ for $Re_\tau = 20\,000$. The smallest-k_x trajectory samples the left/low-κ edge of the kernel and remains at small $\eta = y/h$.

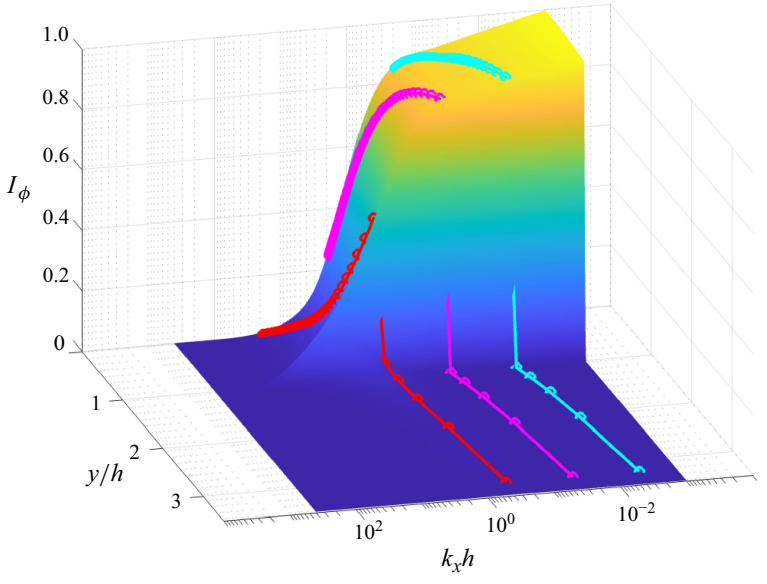


Figure 14. Streamwise energy influence kernel $I_\phi(\kappa_x, \eta)$ (normalized peak value) for hairpin attached eddy at $Re_\tau = 20\,000$.

scale-by-scale contributions from the hairpin attached eddy appear impressive in relation to the inferred quantities.

Physically, low k_x corresponds to very long streamwise wavelengths. In the present attached-eddy framework with independent marks, the low-k_x variance is built by incoherently summing contributions of the largest eddies. In a Poisson superposition, long-wavelength modes are fed by many large eddies with essentially random phases, so variances add without cancellation. Real wall turbulence exhibits organization, intermittency and correlations at the largest scales; those effects can reduce energy in the very lowest modes relative to an independent-eddy superposition. Baars & Marusic (2020*a*, *b*) offer more quantitative insights in the form of three different eddy types, and that attached eddies represent one of these types and contribute a large fraction of the energy only at an intermediate range of scales in the log layer. The latter point has been

https://doi.org/10.1017/jfm.2026.12182 Published online by Cambridge University Press

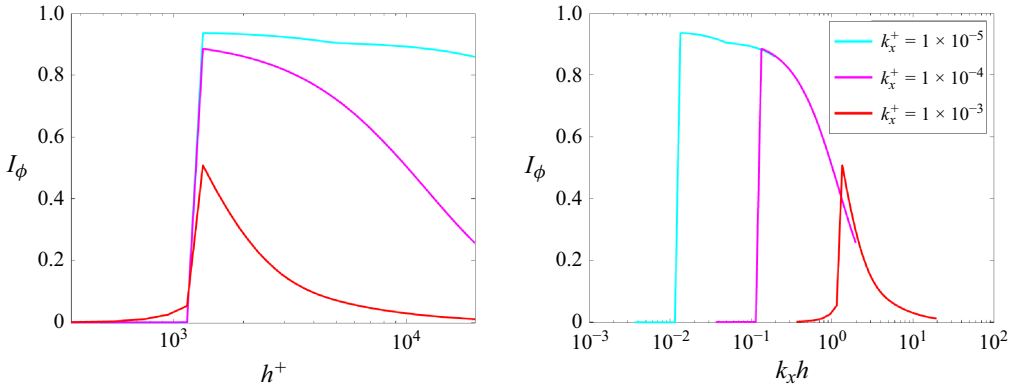


Figure 15. Contribution to F integral from different scales at $y^+ = 1184$ for $Re_\tau = 20\,000$ for hairpin attached eddy.

well argued by Perry & Marušić (1995). The independent-mark hypothesis therefore tends to overpopulate the lowest wavenumbers unless correlations are explicitly modelled or packaged into larger marks. It is possible that the influence kernel I_ϕ can be used in an inverse problem setting to 'design' compositions of prototypical eddies to model desired spectral properties.

5. Why the rectangular hairpin is unusually predictive, and replacing it is difficult

The rectangular hairpin presented above is not just another convenient template that happens to fit well. Rather, it concentrates the entire spanwise displacement at one height, which gives the exact step-shaped mean kernel required by the attached-eddy mean law, while its vertical legs remain spectrally broad and dominate the 1-D streamwise spectrum. In other words, the rectangular hairpin is unusually predictive because it realizes an unusually clean separation of duties. The top segment concentrates the entire spanwise displacement at one height and therefore gives the exact I_1 plateau. The legs carry essentially none of I_1, but because they are strongly localized they dominate most of I_ϕ. The angle θ then tunes the spectral peak largely through phase, without spoiling the mean. Replacing the rectangular hairpin is hard because most alternatives appear to spoil at least one of these properties, and many spoil two of them at once. This was a conclusion reached after a number of optimization attempts on configurations such as those shown in figure 16. The optimization set-up and code can be found at https://github.com/CaslabUM/AttachedEddy.

The author is careful to note that the above statement is not a proof, but a qualitative result. A more rigorous statement can be made in the case of a symmetric three-segment hairpin family whose edge nodes are given by

$$(0,\, 0,\, -b_0/2) \to (\lambda,\, 1,\, -b_1/2) \to (\lambda,\, 1,\, b_1/2) \to (0,\, 0,\, b_0/2). \tag{5.1}$$

Figure 17 shows the geometry in the (y, z) projection.

Appendix C gives individual segment contributions.

Mean contribution. Summing the three segment contributions from (C7) gives the exact single-hairpin mean kernel

$$I_1^{hp}(\eta) = \Gamma\,[b_0 + (b_1 - b_0)\eta]H(1-\eta). \tag{5.2}$$

https://doi.org/10.1017/jfm.2026.12182 Published online by Cambridge University Press

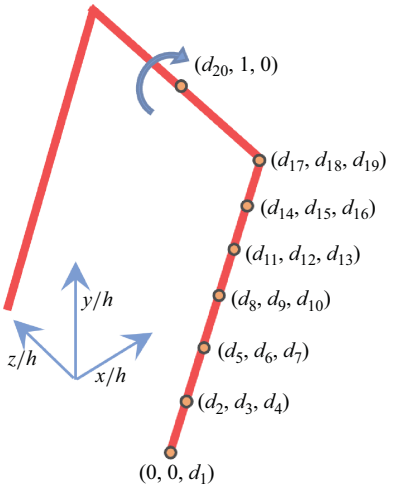


Figure 16. Set-up of a sample optimization study conducted to find an optimal eddy shape. Design variables d_i are coordinate locations which represent the eddy shape. No combination of design variables was found to result in a better prediction of the mean velocity and streamwise variance than the simple rectangular hairpin.

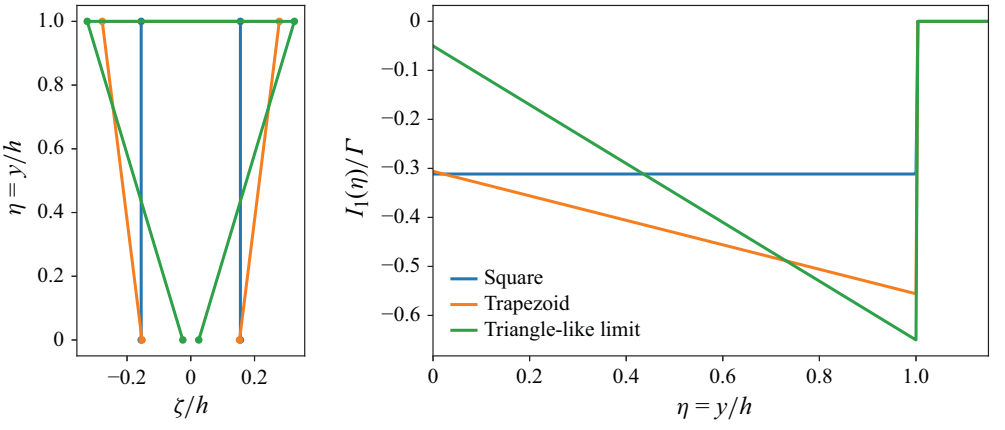


Figure 17. Straight-segment hairpin family and the corresponding exact $I_1(\eta)$ kernels.

This reduces to a plateau when $b_1 = b_0$ and to a ramp when $b_1 \neq b_0$. For the attached-eddy population, the mean profile becomes

$$U^+(y^+) = U^+_{ref} - \beta C \Gamma F_1(y^+), \tag{5.3}$$

with the exact population integral

$$F_1(y^+) = b_0 \log\left(\frac{h^+_{max}}{y^+}\right) + (b_1 - b_0)\left(1 - \frac{y^+}{h^+_{max}}\right), \quad h^+_{min} \leq y^+ \leq h^+_{max}. \tag{5.4}$$

Thus, the rectangular hairpin $b_1 = b_0 = s$ collapses this to the exact logarithmic form

$$F_1(y^+) = s \log(h^+_{max}/y^+) \qquad (h^+_{min} \leq y^+ \leq h^+_{max}). \tag{5.5}$$

This is the main reason the rectangular head remains so predictive: it gives the best possible morphology for the logarithmic mean.

https://doi.org/10.1017/jfm.2026.12182 Published online by Cambridge University Press

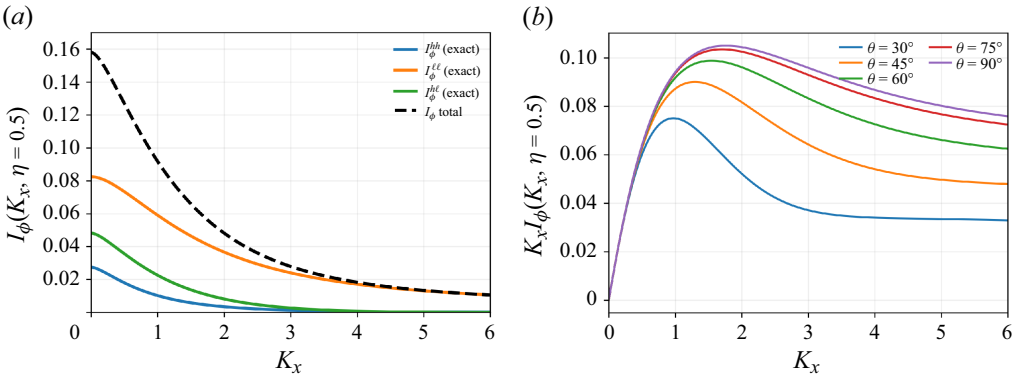


Figure 18. (*a*) Exact square-hairpin decomposition of the single-eddy spectrum into head, leg, and cross contributions at $\eta = 0.5$. (*b*) Premultiplied spectrum for the same square geometry at several inclination angles. The mean kernel is fixed by the top segment, while the angle mainly tunes the spectral peak through the leg phase $e^{-i\kappa_x s \cot\theta}$.

Streamwise kinetic energy. For the rectangular hairpin with $0 < \eta < 1$, Appendix C provides exact expressions for the Fourier transform of the streamwise induced velocities. It is instructive to split the contributions from the head of the hairpin and the legs as $\hat{u}_1 \triangleq \hat{u}_h + \hat{u}_\ell$. Then the spectral kernel can be reduced to an exact quadrature in κ_z:

$$I_\phi^{hh}(\kappa_x, \eta) = \frac{1}{2\pi^2}\int_0^\infty |\widehat{u}_h(\kappa_x, \kappa_z; \eta)|^2 \, \mathrm{d}\kappa_z, \tag{5.6}$$

$$I_\phi^{\ell\ell}(\kappa_x, \eta) = \frac{1}{2\pi^2}\int_0^\infty |\widehat{u}_\ell(\kappa_x, \kappa_z; \eta)|^2 \, \mathrm{d}\kappa_z, \tag{5.7}$$

$$I_\phi^{h\ell}(\kappa_x, \eta) = \frac{1}{\pi^2} Re \int_0^\infty \widehat{u}_h(\kappa_x, \kappa_z; \eta)\, \widehat{u}_\ell(\kappa_x, \kappa_z; \eta)^* \, \mathrm{d}\kappa_z. \tag{5.8}$$

For the representative rectangular hairpin at $\theta = 60°$, and $\eta = 0.5$, these exact formulae give at $\kappa_x = 0$

$$I_\phi^{hh}(0, 0.5) = 2.74 \times 10^{-2}, \quad I_\phi^{\ell\ell}(0, 0.5) = 8.36 \times 10^{-2}, \quad I_\phi^{h\ell}(0, 0.5) = 4.82 \times 10^{-2}. \tag{5.9}$$

This reveals two things: (*a*) the fact that the kernels (and thus ϕ_{xx}) do not decay to zero at zero streamwise wavenumber; and (*b*) even at $\kappa_x = 0$, the head contributes only approximately 17 % of $I_\phi(0)$, the legs contribute approximately 53 %, and the cross term contributes approximately 30 %, even though the head contributes all of I_1. At the premultiplied peak ($\kappa_x \approx 1.55$) the split is approximately 8.5 %, 71.4 % and 20.1 %, and by $\kappa_x = 5$ the legs carry approximately 98.1 % of the spectrum.

This is the sharpest quantitative statement of the mean-variance duality: the head contributes significantly to the mean kernel, but the legs determine most of the spectral energy. As mentioned earlier, the difficulty of replacing the rectangular head is precise rather than qualitative. Any replacement that spreads the top segment over a vertical band immediately destroys the exact plateau in I_1. Triangles, rounded tops, tilted tops and arch-like heads all behave the same way.

The same replacement also changes the head contribution to I_ϕ. Experiments show that downward spreading of the head not only spoils the mean plateau; it also increases the moderate-κ_x head content because part of the head is brought closer to the observation

https://doi.org/10.1017/jfm.2026.12182 Published online by Cambridge University Press

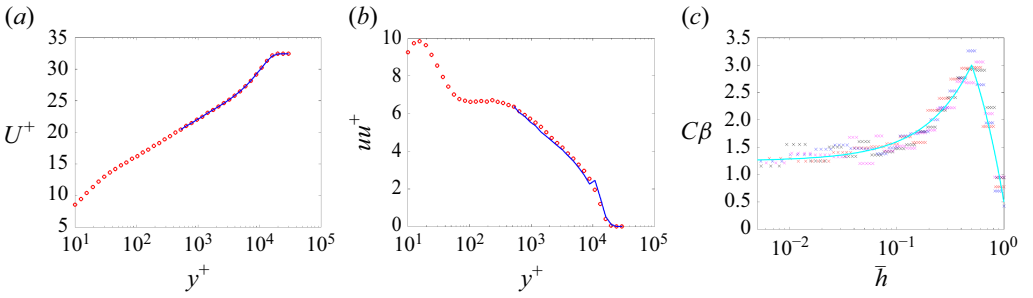


Figure 19. (*a,b*) Joint optimal solution for eddy shape and density at $Re_\tau = 20\,000$. (*c*) Inferred eddy density functions for $Re_\tau = [6000, 10\,000, 14\,500, 20\,000]$ and piecewise linear approximation.

plane. This is exactly the wrong direction if one wants to retain the clean head/leg role separation of the rectangular hairpin.

One might try to keep the top segment at a single height so that I_1 remains exact, and instead replace only the legs. This is a different failure mode. If the legs are broadened, bowed, packetized or rounded in a way that gives them an effective spanwise width w_ℓ, then the mean kernel is still unchanged to leading order because the leg contribution is small, but the spectrum is no longer the same. Even when the mean is preserved exactly, broadening the legs narrows the Cauchy spectrum and shifts the premultiplied peak to lower κ_x. In other words, keeping the right I_1 is not enough: the rectangular hairpin also succeeds because its legs are highly localized and therefore spectrally broad. That is the main reason the rectangular hairpin is unusually predictive: it is one of the very few simple filament templates in which the mean and spectral constraints are nearly decoupled.

6. Inferring and modelling the eddy density

Once the eddy shape is chosen and β is fixed, there are no degrees of freedom left. Yet, the comparisons in the previous section suggest that a minimal hairpin-type eddy can reproduce not only the one-point moments at $Re_\tau \approx 5200$ but also the evolution of U^+, u'^2 and the premultiplied spectrum across Reynolds numbers. This section provides a more substantial interpretation of why this occurs, which ingredients appear essential, and which limitations are inherent to an independent-eddy superposition.

It is useful to separate (i) the population law (β, $p(h)$, h_{min}, h_{max}) from (ii) the single-eddy template (geometry, inclination angle θ, circulation scaling and vortex-core regularization). Under these conventions, the only parameter used to anchor the data is the population amplitude β.

It is, however, possible to improve the accuracy of the model by making the eddy density a function of the eddy size. A joint optimization run was performed for the eddy width, angle and $\beta(h^+)$. The optimization for $Re_\tau = 20\,000$ converged to $\theta = 75°$ and an aspect ratio (ratio of hairpin width and height) of 1.8, and an eddy density as shown in figure 19, which imply that it is possible to get a near-perfect prediction. Keeping the eddy shape and angle fixed, and examining the behaviour of the eddy density function, the following piecewise linear fit was found to be accurate:

$$C\beta(\bar{h}) = \begin{cases} 1.25 + 3.5\bar{h} & 0 \le \bar{h} \le 0.5, \\ 3.0 - 2.5(\bar{h} - 0.5)/0.5 & 0.5 \le \bar{h} \le 1, \end{cases} \tag{6.1}$$

where $\bar{h} = ((h^+ - h^+_{min})/(h^+_{max} - h^+_{min}))$.

https://doi.org/10.1017/jfm.2026.12182 Published online by Cambridge University Press

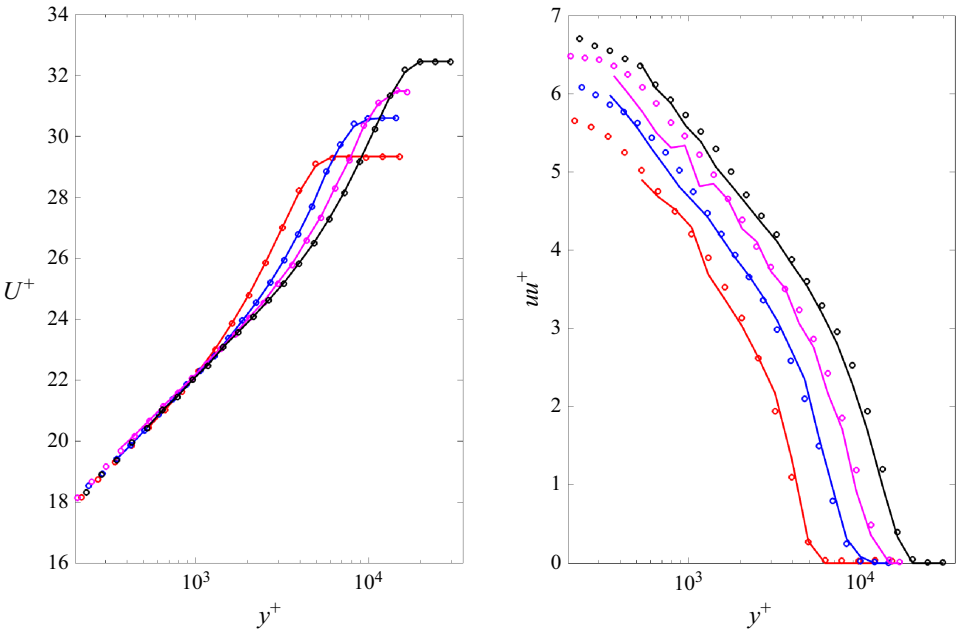


Figure 20. Improved predictions using analytical eddy density function $C\beta(h^+)$ for $Re_\tau = [6000, 10\,000, 14\,500, 20\,000]$.

Physically, the inferred $C\beta(\bar{h})$ peaks at midrange eddy sizes ($\bar{h} \approx 0.5$) and decreases towards both the smallest and largest eddies. This is qualitatively consistent with the expectation that the largest eddies are geometrically constrained by the boundary layer thickness and may be less numerous than a pure $p(h) \propto h^{-3}$ law would predict, while the smallest eddies in the log layer interact with the buffer region where the attached-eddy hypothesis breaks down. However, we note that the piecewise linear form was chosen for simplicity and not derived from physical consistency requirements.

We also note that the jointly optimized angle ($\theta = 75°$) and aspect ratio (1.8) differ from the values used in § 3 ($\theta = 60°$, aspect ratio 1); this suggests that when $\beta(h)$ absorbs additional modelling flexibility, the optimal eddy shape shifts accordingly and the two parameterizations should not be directly compared.

Using this analytical eddy density function, figure 20 shows predictions at 4 different Reynolds numbers.

7. Related approaches and connections

The present work occupies a complementary position within the broader landscape of attached-eddy theories and coherent-structure studies. An important parallel development is the hierarchical random additive process (HRAP) model introduced by Yang *et al.* (2016) which provides an alternative statistical reinterpretation of Townsend's attached-eddy hypothesis. This formulation elegantly recovers logarithmic scaling laws for moments, structure functions, and generalized two-point correlations without requiring explicit specification of eddy geometry. We note that the HRAP framework is a higher level abstraction than the present work, as it encodes only the statistical consequence (additive contributions from a hierarchy of scales) without committing to any particular morphology.

https://doi.org/10.1017/jfm.2026.12182 Published online by Cambridge University Press

Davidson & Krogstad (2009) propose a deliberately simple log-layer model for streamwise fluctuations which reproduces the k_x^{-1} behaviour of the 1-D longitudinal spectrum in the log region and provides reasonable predictions for the variance $u'u'$ (up to an additive constant). The existence and criteria for a k_x^{-1} spectral dependence have been investigated extensively, more recently by Nickels *et al.* (2005). Notably, the k_x^{-1} trend is most apparent very close to the surface, whereas the present comparisons are shown at an intermediate wall-normal distance. The Davidson–Krogstad viewpoint supports the observation that once the mean and a small set of scaling assumptions are fixed, the streamwise spectrum in the log region has limited freedom.

The above works reinforce a key message: different formulations can reproduce expected log-layer statistics. The present work attempts to provide a concrete mechanistic underpinning within a specific formulation of the attached-eddy hypothesis, and thus the conclusions of this study are limited purely to the specific formulation at hand.

The inverse-problem analysis (§ 2) demonstrates that the inferred influence functions $I_1(\eta)$ and $I_{ij}(\eta)$ represent the essential kinematic constraints that any viable eddy must satisfy. As shown in § 5, the rectangular hairpin yields a precise plateau and functions as a minimal template that satisfies these influence-function requirements while remaining consistent with Biot–Savart kinematics and wall boundary conditions.

It is important to distinguish the present statistical/kinematic AEM from the growing body of work that seeks to identify wall-attached eddies as instantaneous, material features in DNS or experimental data. Beginning with del Álamo *et al.* (2006) who identified self-similar vortex clusters in the logarithmic region of turbulent channels, a series of studies have extracted three-dimensional (3-D) coherent structures using various detection criteria. Dennis & Nickels (2011) provided detailed experimental measurements of vortex packets in turbulent boundary layers via tomographic particle image velocimetry. Lozano-Durán *et al.* (2012) characterized the 3-D structure of momentum-transferring Q2/Q4 events, demonstrating that attached structures become geometrically self-similar with sizes proportional to their distance from the wall. More recently, Hwang & Sung (2018) developed a clustering methodology to extract wall-attached structures of velocity fluctuations, and Cheng *et al.* (2019, 2020) employed bidimensional empirical mode decomposition to isolate attached eddies and quantify their contribution to skin-friction generation. Additionally, several studies have demonstrated that statistical properties can be recovered from stochastic representations of eddies with wall-distance scaling (Cuevas Bautista *et al.* 2019; Ehsani *et al.* 2024; Nath & Hickey 2026), and the clustering and larger-scale organization of attached eddies has been investigated by Hutchins *et al.* (2012) and Deshpande *et al.* (2023), among others.

These data-driven approaches validate the physical premise of wall-attached, self-similar hierarchies, providing essential structures that models such as the AEM seek to represent statistically. However, they also reveal complexity that the minimal AEM intentionally abstracts away: instantaneous eddies exhibit significant variability in shape, orientation and internal structure; they interact nonlinearly; and their dynamics involve processes (generation, merging, cascade) not captured by easily interpretable models. The present work thus occupies a middle ground: it provides more geometric specificity than purely statistical models (HRAP) while remaining deliberately simpler than the full complexity revealed by structure-extraction studies. The spectral influence kernel $I_\phi(\kappa_x, \eta)$ introduced in § 4.1 offers a bridge between these perspectives and encodes the spectral signature of a single eddy template and can, in principle, be compared with conditionally averaged spectra from identified structures. Such comparisons, along with extensions to two-dimensional (2-D) (k_x, k_z) spectra and cross-component correlations,

https://doi.org/10.1017/jfm.2026.12182 Published online by Cambridge University Press

represent promising directions for strengthening the connection between kinematic models and data-driven structure identification.

We also note a connection to the resolvent framework (McKeon 2019): the self-similar hierarchy of response modes identified by resolvent analysis shares the same wall-attached scaling as the AEM, and the resolvent modes can be viewed as a dynamically informed basis for the eddies that the AEM treats kinematically. Integrating the spectral influence kernel I_ϕ with resolvent-based predictions of the 2-D spectral tensor represents a promising path towards a dynamically grounded attached-eddy model.

8. Conclusions and perspectives

This work extended the statistical foundations of the attached-eddy modelling framework by clarifying the formulation and offering proofs of convergence. Additional contributions of this work can be summarized as follows.

(i) Inverse problem for attached-eddy kernels. We formulate the recovery of the single-eddy influence functions $I_1(y/h)$ and $I_{ij}(y/h)$ from reference one-point moments as an explicit inverse problem (§ 2). This makes the 'eddy contribution function' a quantitative, inferable object rather than a qualitative sketch.

(ii) Ideal-kernel structure. For the $Re_\tau \approx 5200$ DNS considered, the inferred mean-flow kernel exhibits a near-plateau over $y/h \lesssim 1$ and a transition/decay for $y/h > 1$ (figure 2). This is precisely the structural feature required for logarithmic scaling in (2.4).

(iii) Minimal Biot–Savart-consistent eddy template. A simple rectangular hairpin-type vortex-loop template (implemented with Rankine vortex rods) together with an inviscid image system across the wall can reproduce both the inferred kernels and the corresponding mean and Reynolds-stress profiles with good accuracy (figure 6).

(iv) A spectral influence kernel. We introduce the streamwise-energy influence kernel $I_\phi(\kappa_x, \eta)$ (§ 4.1), which provides a compact representation of how a self-similar eddy footprint populates the 1-D spectrum as a function of scale. The spectral content of a single self-similar eddy as a function of dimensionless wavenumber and relative height is implicit in prior work, possibly dating back to Perry & Chong (1982). In this work, the kernel makes the emergence of the k_x^{-1} scaling band and its limitations explicit, and more transparent than population-level arguments alone and offers insight into constructing more sophisticated compositional eddy models. It is notable that $\int_0^\infty I_\phi(\kappa_x, \eta) d\kappa_x = I_{11}(\eta)$.

(v) Closed-form results for the straight hairpin family. For the three-segment straight-filament hairpin family with wall image, we derive exact expressions for the mean kernel $I_1^{hp}(\eta) = \Gamma[b_0 + (b_1 - b_0)\eta]H(1-\eta)$ (Appendix C, (5.2)), demonstrating that only the rectangular hairpin ($b_1 = b_0$) produces an exact plateau and hence a purely logarithmic mean profile and serves as a minimal eddy that satisfies kinematic constraints and yields acceptable first and second streamwise moment behaviour. Fourier-space expressions for the streamwise velocity (C16) enable an exact head/leg/cross decomposition of the spectral kernel, quantifying the mean-variance duality: for a rectangular hairpin, the head contributes all of I_1 but only $\sim$17 % of I_ϕ at $\kappa_x = 0$ for $\eta = 0.5$, while the legs carry $\sim$53 % of the spectral energy.

(vi) Scale-dependent eddy density. Allowing β to vary with eddy size h provides an additional degree of freedom that yields near-perfect predictions of both mean velocity and streamwise variance across $Re_\tau = 6000$–$20\,000$ (figure 20), with a simple piecewise-linear analytical fit (6.1).

https://doi.org/10.1017/jfm.2026.12182 Published online by Cambridge University Press

The original goal of this work was to use the inferred influence functions to uncover an optimal eddy or packet configuration. One of the conclusions of this work is that a simple Rankine rod-based rectangular hairpin is unusually predictive once the mean is anchored, and is able to represent attached-eddy physics. The reasons are as follows:

(i) The single-eddy spectrum is determined by $I_\phi(\kappa_x, \eta)$, a two-variable kernel. Population integration introduces only the scale window and one amplitude constant (β).
(ii) Here $p(h) \propto h^{-3}$ cancels the h^3 prefactor exactly. This produces the $1/k_x$ factor explicitly and shifts the remaining complexity into the slowly varying integral $F(k_x; y)$.
(iii) The tilted hairpin footprint produces streamwise-extended u signatures on a wall-parallel plane. Through the $k_x h$ mapping, the dominant wavelengths at y are in the decade $\lambda_x = O(10y)$, which at $y^+ \sim 10^3$ sits near $\lambda_x^+ \sim 10^4$.
(iv) Reynolds number variation enters mainly through the window endpoints. For fixed y^+ in the log region, changing Re_τ changes h_{max} and therefore the low-k_x limit, while leaving much of the intermediate band governed by the same kernel shape.

At this juncture, we remark that the AEM is a statistical and non-dynamic model, and thus prototypical eddies cannot be interpreted as literal material structures, even if they provide useful building blocks for kinematic prediction. Nevertheless, the inverse-kernel viewpoint provides a bridge between statistical requirements (what kernels are needed to match moments) and geometric hypotheses (what minimal eddy templates can realize those kernels under Biot–Savart induction). A good fit of a 1-D premultiplied spectrum does not uniquely identify a specific structure. Many different eddy templates can generate similar k^{-1}-like behaviour once integrated over a scale-invariant population. Therefore, the fact that the Rankine-rod hairpin AEM matches experiments across many quantities of interest and Reynolds numbers is encouraging, but it is not, by itself, a proof that the flow is literally composed of those hairpins. Stronger discrimination can come from tests that 1-D spectra smear out: 2-D spectra, cross-spectra, coherence, wall-normal and spanwise components, vorticity-related spectra and conditional structure signatures. It is noted that while statistical results are presented only in the logarithmic region, where attached eddies are predominant, the integration limits span the bottom of the log layer all the way to the boundary layer height, where detached eddies persist. Future work may examine the sensitivity of the results to the limits of integration, and additional models for detached eddies.

Inverse problems as a pathway forward. The inverse formulation suggests several immediate extensions: (i) simultaneous inference of multiple kernels using multiple moments and multiple Reynolds numbers with shared regularization and physically motivated constraints, (ii) inference of 2-D spectral kernels (in (k_x, k_z)) rather than only 1-D kernels and (iii) incorporation of non-Poisson population effects (packets, clustering, exclusion) through pair-correlation corrections to (1.15) and their spectral counterparts. A key limitation of the present validation is that it is restricted to the streamwise velocity component: the mean U^+, the streamwise variance $\overline{u'^2}$ and the 1-D streamwise energy spectrum. Extending the comparisons to all components of the Reynolds stress tensor (wall-normal and spanwise variances and the Reynolds shear stress), two-point correlations and 2-D (k_x, k_z) spectra would provide a much more stringent test of the minimal eddy hypothesis and could distinguish between eddy templates that appear equivalent in 1-D metrics.

https://doi.org/10.1017/jfm.2026.12182 Published online by Cambridge University Press

Acknowledgements. This work was supported by the Aeronautics Research Mission Directorate at NASA through the Transformative Aeronautical Concepts Program (TACP) and the D.2 Transformational Tools and Technologies Project (TTT) under contract # 80NSSC23M0215. Early part of the research was supported by NASA grant # 80NSSC18M0149. The analytical expressions in (36)–(39) were derived with the help of GPT5.2-Pro from OpenAI, Inc.

Declaration of interests. The author reports no conflict of interest.

Appendix A. Numerical convergence

Let $\rho \triangleq \sqrt{\xi^2 + \zeta^2}$. A standard sufficient condition for convergence is that

$$\int_{\mathbb{R}^2} |u_1(\xi, \zeta, \eta)| \, \mathrm{d}\xi \, \mathrm{d}\zeta < \infty. \tag{A1}$$

A convenient and interpretable sufficient condition is a power-law far-field bound $|u_1(\xi, \zeta, \eta)| \leq C(\eta)\,(1+\rho)^{-p}$ for some $p > 2$. Indeed, the tail can be bounded (up to an angular factor) by

$$\left|I_1(\eta) - I_1(\eta; R)\right| \leq \int_{\rho > R} |u_1| \, \mathrm{d}A \lesssim 2\pi C(\eta) \int_R^\infty \rho^{1-p} \, \mathrm{d}\rho = \frac{2\pi C(\eta)}{p-2} R^{2-p}. \tag{A2}$$

Hence, $p > 2$ guarantees convergence as $R \to \infty$. The borderline case $p = 2$ produces a logarithmic divergence $\sim \log R$; for $p = 3$ the tail decays as $O(1/R)$.

Reynolds-stress kernels are less restrictive. Similarly, the second-moment influence functions are

$$I_{ij}(\eta; R) \triangleq \int_{-R}^{R} \int_{-R}^{R} u_i(\xi, \zeta, \eta)\, u_j(\xi, \zeta, \eta) \, \mathrm{d}\xi \, \mathrm{d}\zeta, \qquad I_{ij}(\eta) \triangleq \lim_{R \to \infty} I_{ij}(\eta; R), \tag{A3}$$

whenever the limit exists. A sufficient condition for I_{ij} to be well-defined is $u_i(\cdot, \cdot, \eta)\, u_j(\cdot, \cdot, \eta) \in L^1(\mathbb{R}^2)$. If each velocity component satisfies the far-field decay $|u_k| \lesssim \rho^{-p}$, then $u_i u_j \lesssim \rho^{-2p}$, and the planar tail behaves like $\int_R^\infty \rho\, \rho^{-2p} \, \mathrm{d}\rho = \int_R^\infty \rho^{1-2p} \, \mathrm{d}\rho$, which converges whenever $p > 1$. Thus, the convergence requirement for the mean-flow influence I_1 (which requires $p > 2$) is typically the more restrictive requirement; once I_1 is well-defined, the second-moment kernels I_{ij} are generally well-defined for the same eddy field.

Implications for Biot–Savart line-vortex eddies and the role of the image system. For line-vortex Biot–Savart fields, a generic open filament can generate a ρ^{-2} contribution to certain velocity components in the far field, which is precisely the borderline case for I_1 and would lead to a logarithmic growth of $I_1(\eta; R)$ with R. The specific square-hairpin eddy used herein is paired with an opposite-sign mirror image across $y = 0$ (to enforce inviscid wall boundary conditions), and the wall-parallel segment cancels with its image. This construction removes leading-order contributions responsible for a ρ^{-2} tail in the streamwise component and yields a faster far-field decay. In other words, the image construction is not a technical convenience: it is central to ensuring that (1.6) is well posed for a line-vortex eddy model.

Numerical evidence. To verify the decay/convergence directly, we performed a Biot–Savart calculation for a simple rectangular hairpin (three straight segments with unit circulation) together with an opposite-sign mirror image across $y = 0$, consistent with the construction described around figure 5. A small vortex-core regularization was used to smooth the near-filament singularity; this does not affect the far-field decay that controls convergence of the planar integrals.

https://doi.org/10.1017/jfm.2026.12182 Published online by Cambridge University Press

$R = L/h$	$I_1(\eta = 0.5;\, R)$
4	−0.885
8	−0.941
12	−0.960
16	−0.969
20	−0.975
24	−0.979

Table 1. Convergence of the planar influence integral $I_1(\eta;\, R)$ for the rectangular hairpin + image at $\eta = 0.5$.

Far-field decay check. At $\eta = y/h = 0.5$, evaluating along $(\xi, 0, \eta)$ with $\xi \gg 1$ gives

$$\begin{aligned} u_1(10, 0, 0.5) &\approx -3.92 \times 10^{-4}, \\ u_1(20, 0, 0.5) &\approx -4.44 \times 10^{-5}, \\ u_1(40, 0, 0.5) &\approx -5.26 \times 10^{-6}, \\ u_1(80, 0, 0.5) &\approx -6.39 \times 10^{-7}. \end{aligned} \tag{A4}$$

Moreover, $u_1(\xi, 0, 0.5)\, \xi^3$ is approximately constant (between ≈ -0.33 and ≈ -0.39), indicating the scaling

$$u_1(\rho, \eta) \sim \frac{C(\eta)}{\rho^3} \qquad (\rho \to \infty), \tag{A5}$$

so that $\left|I_1(\eta) - I_1(\eta;\, R)\right| = O(1/R)$ as predicted by (A2) with $p = 3$.

Direct growth of I_1 with domain size. For the same hairpin at $\eta = 0.5$, integrating over $[-R,\, R]^2$ yields the values shown in table 1. The observed approach is consistent with the $O(1/R)$ tail implied by (A5). In particular, extrapolating with the model $I_1(\eta;\, R) = I_{1,\infty}(\eta) + C/R$ gives

$$I_{1,\infty}(\eta = 0.5) \approx -0.997. \tag{A6}$$

Above the eddy in this toy geometry, the convergence is rapid; e.g. at $\eta = 1.2$, $I_1(1.2;\, R)$ approaches 0 quickly (with $I_1 \approx 0.005$ by $R = 24$), again consistent with a well-defined infinite-domain limit.

Practical implication for the homogenization argument. In the attached-eddy homogenization step, taking L/h 'large enough' should be interpreted as choosing $R = L/h$ such that the residual tail $\left|I_1(\eta) - I_1(\eta;\, R)\right|$ (and similarly for I_{ij}) is negligible at the level of accuracy desired. For the line-vortex eddies considered here, this condition is satisfied because the image construction yields a sufficiently rapid far-field decay of the induced streamwise velocity, ensuring that the planar influence integrals are well-defined in the limit $R \to \infty$.

Appendix B. Components of the inverse kernel optimization

More details are provided on the construction of the matrices involved in (4.9).

Construction of the forward matrix A. For each measurement pair (i, j) and each quadrature node h_q, define

$$\eta_{iq} = \frac{y_i}{h_q}, \qquad \kappa_{ijq} = k_{x,j} h_q. \tag{B1}$$

https://doi.org/10.1017/jfm.2026.12182 Published online by Cambridge University Press

If $(\kappa_{ijq}, \eta_{iq})$ lies outside the inversion grid, that contribution is skipped. Otherwise, the kernel value is obtained by bilinear interpolation on the logarithmic coordinate grid $\xi = \log\kappa$, $\zeta = \log\eta$. Given $\kappa_a \le \kappa_{ijq} \le \kappa_{a+1}$, $\eta_b \le \eta_{iq} \le \eta_{b+1}$. The local interpolation coordinates are

$$t_\kappa = \frac{\log\kappa_{ijq} - \log\kappa_a}{\log\kappa_{a+1} - \log\kappa_a}, \quad t_\eta = \frac{\log\eta_{iq} - \log\eta_b}{\log\eta_{b+1} - \log\eta_b}. \tag{B2}$$

The four bilinear weights are then

$$\omega^{00}_{ijq} = w_q(1-t_\kappa)(1-t_\eta), \quad \omega^{10}_{ijq} = w_q t_\kappa(1-t_\eta), \quad \omega^{01}_{ijq} = w_q(1-t_\kappa)t_\eta, \quad \omega^{11}_{ijq} = w_q t_\kappa t_\eta. \tag{B3}$$

If row m corresponds to (i, j), these weights are accumulated into the sparse matrix as

$$A_{m,\ell(b,a)} \mathrel{+}= \omega^{00}_{ijq}, \quad A_{m,\ell(b,a+1)} \mathrel{+}= \omega^{10}_{ijq}, \quad A_{m,\ell(b+1,a)} \mathrel{+}= \omega^{01}_{ijq}, \quad A_{m,\ell(b+1,a+1)} \mathrel{+}= \omega^{11}_{ijq}. \tag{B4}$$

Therefore each matrix row represents the quadrature approximation

$$(A\boldsymbol{x})_m \approx \sum_{q=1}^{n_h} w_q\, \mathcal{I}_{log}[\psi](\kappa_{ijq}, \eta_{iq}), \tag{B5}$$

where $\mathcal{I}_{log}$ denotes bilinear interpolation on the $(\log\kappa, \log\eta)$ grid. For the present inversion, $\boldsymbol{A} \in \mathbb{R}^{11327\times5712}$, $\mathrm{nnz}(\boldsymbol{A}) = 990659$.

Regularization matrices. The inversion uses second-difference smoothness penalties in both coordinate directions plus a very small minimum-norm term. First define the standard second-difference matrix

$$\boldsymbol{D}_n = \begin{bmatrix} 1 & -2 & 1 & 0 & \cdots & 0 \\ 0 & 1 & -2 & 1 & \cdots & 0 \\ \vdots & & \ddots & \ddots & \ddots & \vdots \\ 0 & \cdots & 0 & 1 & -2 & 1 \end{bmatrix} \in \mathbb{R}^{(n-2)\times n}. \tag{B6}$$

Then the two directional penalties are built by Kronecker products:

$$\boldsymbol{L}_\kappa = I_{n_\eta} \otimes D_{n_\kappa}, \quad \boldsymbol{L}_\eta = D_{n_\eta} \otimes I_{n_\kappa}, \quad \boldsymbol{L}_0 = I_{n_\eta n_\kappa}. \tag{B7}$$

Their dimensions used were

$$\boldsymbol{L}_\kappa \in \mathbb{R}^{5544\times5712}, \quad \boldsymbol{L}_\eta \in \mathbb{R}^{5576\times5712}, \quad \boldsymbol{L}_0 \in \mathbb{R}^{5712\times5712}. \tag{B8}$$

Construction of vector **b**. Each usable spectrum sample becomes one entry of the right-hand side. If measurement index m corresponds to wall-normal location y_i and streamwise wavenumber $k_{x,j}$, then $b_m = \widehat{\Phi}_{ij}$. The implementation only retains points satisfying

$$\widehat{\Phi}_{ij} > 0, \qquad k_{x,j} > 0, \qquad \text{all quantities finite.} \tag{B9}$$

Appendix C. Analytical expressions for single straight filament with image

Let a straight segment run from

$$A = (\xi_a, \eta_a, \zeta_a), \qquad B = (\xi_b, \eta_b, \zeta_b), \tag{C1}$$

with circulation Γ, and let the wall image be the reflected segment

$$A' = (\xi_a, -\eta_a, \zeta_a), \qquad B' = (\xi_b, -\eta_b, \zeta_b) \tag{C2}$$

https://doi.org/10.1017/jfm.2026.12182 Published online by Cambridge University Press

of circulation $-\Gamma$. Define $\Delta\xi = \xi_b - \xi_a$, $\Delta\eta = \eta_b - \eta_a$, $\Delta\zeta = \zeta_b - \zeta_a$. The segment is parameterized as $\boldsymbol{r}(s) = A + s(B - A), \quad 0 \le s \le 1$.

Exact formula for $I_1(\eta)$. The planar mean kernel is $I_1(\eta) = \int_{\mathbb{R}^2} u_1(\xi, \eta, \zeta)\, \mathrm{d}\xi\, \mathrm{d}\zeta$. Using the vorticity $\omega_z = \partial_x u_2 - \partial_y u_1$ and integrating over the wall-parallel plane gives

$$\frac{\mathrm{d}I_1}{\mathrm{d}\eta} = -\int_{\mathbb{R}^2} \omega_z(\xi, \eta, \zeta)\, \mathrm{d}\xi\, \mathrm{d}\zeta. \tag{C3}$$

For one filament,

$$\omega_z = \Gamma \int_0^1 \delta(\boldsymbol{x} - \boldsymbol{r}(s))\, \zeta'(s)\, \mathrm{d}s, \tag{C4}$$

so

$$I_1(\eta) = \Gamma \int_0^1 H(\eta(s) - \eta)\, \zeta'(s)\, \mathrm{d}s. \tag{C5}$$

For the straight segment, $\zeta'(s) = \Delta\zeta$ and $\eta(s) = \eta_a + s\Delta\eta$, hence

$$I_1^{AB}(\eta) = \Gamma\, \Delta\zeta \int_0^1 H(\eta_a + s\Delta\eta - \eta)\, \mathrm{d}s. \tag{C6}$$

If $\Delta\eta \neq 0$, this evaluates to

$$I_1^{AB}(\eta) = \Gamma\, \Delta\zeta\, \frac{(\eta_+ - \eta)_+ - (\eta_- - \eta)_+}{\eta_+ - \eta_-}, \tag{C7}$$

where

$$\eta_+ = \max(\eta_a, \eta_b), \qquad \eta_- = \min(\eta_a, \eta_b), \qquad (q)_+ = \max(q, 0). \tag{C8}$$

If $\Delta\eta = 0$, the segment is horizontal in the (y, z) projection and

$$I_1^{AB}(\eta) = \Gamma\, \Delta\zeta\, H(\eta_a - \eta). \tag{C9}$$

For a physical segment entirely in $y > 0$, the image contribution vanishes identically for $\eta > 0$, so the wall-inclusive I_1 is exactly the same as (C7)–(C9). This is the key simplification for optimization: I_1 depends only on the projected trace in the (y, z) plane.

Closed form for $\widehat{u}_1(k_x, \eta, k_z)$. Define

$$\widehat{u}_1(k_x, \eta, k_z) \triangleq \int_{\mathbb{R}^2} u_1(\xi, \eta, \zeta) e^{-i(k_x\xi + k_z\zeta)}\, \mathrm{d}\xi\, \mathrm{d}\zeta, \qquad q = \sqrt{k_x^2 + k_z^2}. \tag{C10}$$

The partial Fourier transform of Biot–Savart for a filament segment plus image gives

$$\begin{aligned}\widehat{u}_1 = \frac{\Gamma}{2} \int_0^1 e^{-i(k_x\xi(s) + k_z\zeta(s))} \Big[&(\zeta' - i\eta' k_z/q) e^{-q(\eta(s) - \eta)} H(\eta(s) - \eta) \\ &- (\zeta' + i\eta' k_z/q) e^{-q(\eta - \eta(s))} H(\eta - \eta(s)) + (\zeta' - i\eta' k_z/q) e^{-q(\eta + \eta(s))} \Big] \mathrm{d}s.\end{aligned} \tag{C11}$$

For a straight segment, the phase is linear,

$$\alpha = k_x\Delta\xi + k_z\Delta\zeta, \qquad k_x\xi(s) + k_z\zeta(s) = k_x\xi_a + k_z\zeta_a + \alpha s. \tag{C12}$$

https://doi.org/10.1017/jfm.2026.12182 Published online by Cambridge University Press

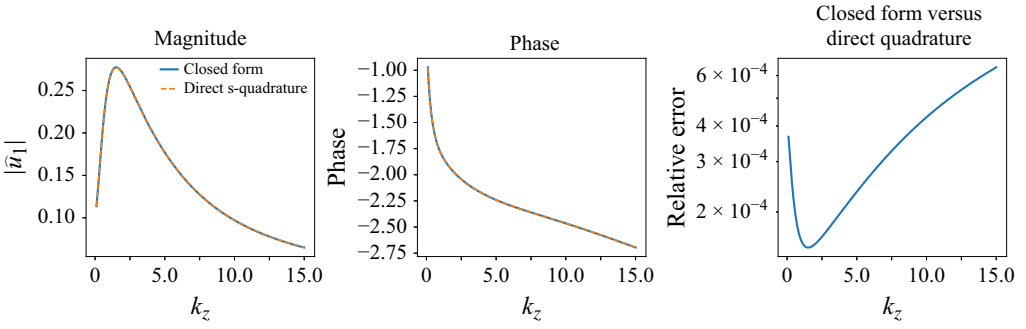


Figure 21. Validation of the closed-form straight-segment transform against direct quadrature in the segment parameter s.

It is convenient to define

$$J_+(s_0, s_1) \triangleq \int_{s_0}^{s_1} e^{-i\alpha s} e^{-q(\eta_a + s\Delta\eta - \eta)}\, \mathrm{d}s = e^{-q(\eta_a-\eta)} \frac{e^{-(q\Delta\eta + i\alpha)s_0} - e^{-(q\Delta\eta+i\alpha)s_1}}{q\Delta\eta + i\alpha}, \tag{C13}$$

$$J_-(s_0, s_1) \triangleq \int_{s_0}^{s_1} e^{-i\alpha s} e^{-q(\eta - \eta_a - s\Delta\eta)}\, \mathrm{d}s = e^{-q(\eta-\eta_a)} \frac{e^{(q\Delta\eta - i\alpha)s_1} - e^{(q\Delta\eta-i\alpha)s_0}}{q\Delta\eta - i\alpha}, \tag{C14}$$

$$J_{img} \triangleq \int_0^1 e^{-i\alpha s} e^{-q(\eta + \eta_a + s\Delta\eta)}\, \mathrm{d}s = e^{-q(\eta+\eta_a)} \frac{1 - e^{-(q\Delta\eta+i\alpha)}}{q\Delta\eta + i\alpha}. \tag{C15}$$

Then

$$\widehat{u}_1 = \frac{\Gamma}{2} e^{-i(k_x\xi_a + k_z\zeta_a)} \Big[(\Delta\zeta - i\,\Delta\eta\, k_z/q) J_+ - (\Delta\zeta + i\,\Delta\eta\, k_z/q) J_- + (\Delta\zeta - i\,\Delta\eta\, k_z/q) J_{img} \Big], \tag{C16}$$

where the interval used in J_+ and J_- depends on whether the segment is above, below or cut by the plane $y = \eta$. If $s_\eta = (\eta - \eta_a)/\Delta\eta$ lies inside $(0, 1)$, the physical segment is split into $[0, s_\eta]$ and $[s_\eta, 1]$. Figure 21 validates the closed form against direct quadrature of (C11) for a generic segment.

Appendix D. Why I_{11}, and hence uu^+, are logarithmic

Let $I_\phi(\kappa, \eta)$ denote the single-eddy streamwise spectral kernel, with $\kappa = k_x h$ and $\eta = y/h$. The corresponding single-eddy second-moment kernel is

$$I_{11}(\eta) = \int_0^\infty I_\phi(\kappa, \eta)\, \mathrm{d}\kappa. \tag{D1}$$

In the attached-eddy hierarchy,

$$R_{11}(y) = \overline{u'^2}(y) = \beta \int_{h_{min}}^{h_{max}} p(h)\, h^2\, I_{11}(y/h)\, \mathrm{d}h. \tag{D2}$$

For the scale-invariant population law $p(h) = Ch^{-3}$, this becomes $R_{11}(y) = \beta C \int_{y/h_{max}}^{y/h_{min}} ((I_{11}(\eta))/\eta)\, \mathrm{d}\eta$. Therefore the criterion for a logarithm in $uu^+ = R_{11}/u_\tau^2$ is

https://doi.org/10.1017/jfm.2026.12182 Published online by Cambridge University Press

simple: if $I_{11}(\eta)$ is approximately constant for $0 < \eta \lesssim 1$, then

$$R_{11}(y) \sim \log\left(\frac{h_{max}}{y}\right), \qquad uu^{+}(y) = B_1 - A_1 \log(y/\delta), \tag{D3}$$

with $h_{max} \sim \delta$ and $A_1 = ((\beta C b_0)/u_\tau^2)$, $b_0 \approx I_{11}(\eta < 1)$. The issue is therefore reduced to the behaviour of $I_{11}(\eta)$.

For the validated rectangular hairpin surrogate at $\eta = 0.5$, $I_\phi(\kappa, 0.5) \approx I_\phi^{(hh)}(\kappa, 0.5) + I_\phi^{(\ell\ell)}(\kappa, 0.5) + I_\phi^{(h\ell)}(\kappa, 0.5)$, with

$$I_\phi^{(hh)}(\kappa, 0.5) \approx 0.0296 e^{-1.058\kappa}, \tag{D4}$$

$$I_\phi^{(\ell\ell)}(\kappa, 0.5) \approx \frac{0.0812}{\left[1 + (\kappa/1.276)^2\right]^{0.651}}, \tag{D5}$$

$$I_\phi^{(h\ell)}(\kappa, 0.5) \approx \frac{0.0495 e^{-0.525\kappa}}{\left[1 + (\kappa/2.096)^2\right]^{1.208}}. \tag{D6}$$

Because this validation is explicit on the resolved band $0 \le \kappa \le 4.5$, define

$$I_{11,4.5}(0.5) \triangleq \int_0^{4.5} I_\phi(\kappa, 0.5)\, \mathrm{d}\kappa. \tag{D7}$$

Then

$$I_{11,4.5}(0.5) = I_{11,4.5}^{(hh)}(0.5) + I_{11,4.5}^{(\ell\ell)}(0.5) + I_{11,4.5}^{(h\ell)}(0.5). \tag{D8}$$

The head contribution:

$$I_{11,4.5}^{(hh)}(0.5) = 0.0296 \int_0^{4.5} e^{-1.058\kappa}\, \mathrm{d}\kappa = 0.0296 \frac{1 - e^{-1.058 \cdot 4.5}}{1.058} \approx 0.0277. \tag{D9}$$

The other two surrogate integrals give

$$I_{11,4.5}^{(\ell\ell)}(0.5) \approx 0.177, \qquad I_{11,4.5}^{(h\ell)}(0.5) \approx 0.0569. \tag{D10}$$

Hence $I_{11,4.5}(0.5) \approx 0.262$.

So the dominant contribution to I_{11} comes from the broad leg spectrum, not from the head. To see how this persists with η, use the componentwise continuation

$$I_\phi^{(hh)}(\kappa, \eta) \approx A_h(\eta) e^{-2\kappa d_{eff}(\eta)}, \qquad d_{eff}(\eta) \approx 1 - \eta, \tag{D11}$$

and

$$I_\phi^{(\ell\ell)}(\kappa, \eta) \approx A_\ell(\eta) \frac{\kappa^{p_\ell(\eta)}}{\left[1 + (\kappa/\kappa_{0,\ell}(\eta))^2\right]^{q_\ell(\eta)}}. \tag{D12}$$

The leg contribution to I_{11} is then explicit:

$$I_{11}^{(\ell\ell)}(\eta) \approx A_\ell(\eta) \int_0^{\infty} \frac{\kappa^{p_\ell(\eta)}}{\left[1 + (\kappa/\kappa_{0,\ell}(\eta))^2\right]^{q_\ell(\eta)}}\, \mathrm{d}\kappa. \tag{D13}$$

With the change of variable $t = (\kappa/\kappa_{0,\ell})^2$,

$$I_{11}^{(\ell\ell)}(\eta) \approx \frac{A_\ell(\eta)\, \kappa_{0,\ell}(\eta)^{1+p_\ell(\eta)}}{2} \int_0^{\infty} t^{(p_\ell(\eta)-1)/2} (1+t)^{-q_\ell(\eta)}\, \mathrm{d}t. \tag{D14}$$

https://doi.org/10.1017/jfm.2026.12182 Published online by Cambridge University Press

Therefore

$$I_{11}^{(\ell\ell)}(\eta) \approx \frac{A_\ell(\eta)\,\kappa_{0,\ell}(\eta)^{1+p_\ell(\eta)}}{2} B\left(\frac{1+p_\ell(\eta)}{2}, q_\ell(\eta) - \frac{1+p_\ell(\eta)}{2}\right), \tag{D15}$$

provided

$$q_\ell(\eta) > \frac{1+p_\ell(\eta)}{2}, \tag{D16}$$

which is satisfied by the fitted parameters. Using the fitted values

$$(\eta,\, A_\ell,\, p_\ell,\, \kappa_{0,\ell},\, q_\ell) = (0.2,\, 0.082,\, -0.03,\, 1.64,\, 0.88), \tag{D17}$$

$$(0.5,\, 0.072,\, -0.04,\, 1.70,\, 0.87), \tag{D18}$$

$$(0.7,\, 0.059,\, -0.05,\, 1.74,\, 0.82), \tag{D19}$$

$$(0.9,\, 0.040,\, -0.06,\, 1.54,\, 0.70), \tag{D20}$$

one obtains $I_{11}^{(\ell\ell)}(0.2) \approx 0.251$, $I_{11}^{(\ell\ell)}(0.5) \approx 0.230$, $I_{11}^{(\ell\ell)}(0.7) \approx 0.211$, $I_{11}^{(\ell\ell)}(0.9) \approx 0.173$.

Thus, the dominant part of $I_{11}(\eta)$ stays roughly constant for $0 < \eta < 1$. This is the structure needed in the attached-eddy integral,

$$I_{11}(\eta) \approx b_0 \qquad (0 < \eta \lesssim 1), \tag{D21}$$

so that

$$R_{11}(y) = \beta C \int_{y/h_{max}}^{y/h_{min}} \frac{I_{11}(\eta)}{\eta}\,\mathrm{d}\eta \approx \beta C b_0 \int_{y/h_{max}}^{\eta_*} \frac{\mathrm{d}\eta}{\eta} + \text{const}, \tag{D22}$$

and therefore

$$R_{11}(y) \approx \beta C b_0 \log\left(\frac{\eta_* h_{max}}{y}\right) + \text{const}. \tag{D23}$$

Thus,

$$uu^+(y) = B_1 - A_1 \log(y/\delta), \qquad A_1 = \frac{\beta C b_0}{u_\tau^2}. \tag{D24}$$

This asymmetry in the tolerance applied to I_1 and I_{11} reflects a corresponding asymmetry in the evidence each is required to reproduce. A clear logarithmic region in the mean velocity is established at Reynolds numbers for which the streamwise variance exhibits no comparable region: the variance instead displays an extended plateau (e.g. figure 19), and a logarithmic decay emerges only at substantially higher Re_τ with a weaker slope (see, for instance, figure 9 in Samie *et al.* (2018)).The mean profile therefore constrains the kernel considerably more tightly than the second moment does.

The logarithm in the mean comes from the exact step in I_1, whereas the logarithm in uu^+ comes from the approximately constant, leg-dominated second-moment kernel I_{11}. In the rectangular hairpin, the head carries the mean, but the legs carry most of the variance. It is noted that for $0 \le \eta \le 1$, I_1 is precisely constant, whereas I_{11} is only approximately constant.

Using the fitted leg parameters and the population constants from the $\theta = 60°$ rectangular hairpin model, one obtains $A_1 \approx 1.2$, consistent with the experimentally observed slope reported by Marusic *et al.* (2013). This provides an independent

https://doi.org/10.1017/jfm.2026.12182 Published online by Cambridge University Press

consistency check linking the spectral structure of the minimal eddy to the observed log–linear decay of the streamwise variance.

References

Baars, W.J. & Marusic, I. 2020*a* Data-driven decomposition of the streamwise turbulence kinetic energy in boundary layers. Part 1. Energy spectra. *J. Fluid Mech.* **882**, A25.

Baars, W.J. & Marusic, I. 2020*b* Data-driven decomposition of the streamwise turbulence kinetic energy in boundary layers. Part 2. Integrated energy and. *J. Fluid Mech.* **882**, A26.

Bautista, C., Carlos, J., Ebadi, A., White, C.M., Chini, G.P. & Klewicki, J.C. 2019 A uniform momentum zone–vortical fissure model of the turbulent boundary layer. *J. Fluid Mech.* **858**, 609–633.

Buccini, A., Chen, F., Pasha, M. & Reichel, L. 2025 Krylov subspace based fista-type methods for linear discrete ill-posed problems. *Numer. Linear Algebra Appl.* **32** (1), e2610.

Cheng, C., Li, W., Lozano-Durán, A. & Liu, H. 2019 Identity of attached eddies in turbulent channel flows with bidimensional empirical mode decomposition. *J. Fluid Mech.* **870**, 1037–1071.

Cheng, C., Li, W., Lozano-Durán, A. & Liu, H. 2020 Uncovering Townsend's wall-attached eddies in low-Reynolds-number wall turbulence. *J. Fluid Mech.* **889**, A29.

Davidson, P.A. & Krogstad, P.-Å. 2009 A simple model for the streamwise fluctuations in the log-law region of a boundary layer. *Phys. Fluids* **21** (5), 055105.

Davidson, P.A., Nickels, T.B. & Krogstad, P.-Å. 2006 The logarithmic structure function law in wall-layer turbulence. *J. Fluid Mech.* **550**, 51–60.

del Álamo, J.C., Jiménez, J., Zandonade, P. & Moser, R.D. 2006 Self-similar vortex clusters in the turbulent logarithmic region. *J. Fluid Mech.* **561**, 329–358.

Dennis, D.J.C. & Nickels, T.B. 2011 Experimental measurement of large-scale three-dimensional structures in a turbulent boundary layer. Part 1. Vortex packets. *J. Fluid Mech.* **673**, 180–217.

Deshpande, R., van den Bogaard, A., Vinuesa, R., Lindić, L. & Marusic, I. 2023 Reynolds-number effects on the outer region of adverse-pressure-gradient turbulent boundary layers. *Phys. Rev. Fluids* **8** (12), 124604.

de Silva, C.M., Hutchins, N. & Marusic, I. 2016*a* Uniform momentum zones in turbulent boundary layers. *J. Fluid Mech.* **786**, 309–331.

de Silva, C.M., Woodcock, J.D., Hutchins, N. & Marusic, I. 2016*b* Influence of spatial exclusion on the statistical behavior of attached eddies. *Phys. Rev. Fluids* **1** (2), 022401.

Ehsani, R., Heisel, M., Li, J., Voller, V., Hong, J. & Guala, M. 2024 Stochastic modelling of the instantaneous velocity profile in rough-wall turbulent boundary layers. *J. Fluid Mech.* **979**, A12.

Hutchins, N., Chauhan, K., Marusic, I., Monty, J. & Klewicki, J. 2012 Towards reconciling the large-scale structure of turbulent boundary layers in the atmosphere and laboratory. *Boundary-Layer Meteorol.* **145** (2), 273–306.

Hwang, Y. & Eckhardt, B. 2020 Attached eddy model revisited using a minimal quasi-linear approximation. *J. Fluid Mech.* **894**, A23.

Hwang, J. & Sung, H.J. 2018 Wall-attached structures of velocity fluctuations in a turbulent boundary layer. *J. Fluid Mech.* **856**, 958–983.

Lee, M. & Moser, R.D. 2015 Direct numerical simulation of turbulent channel flow up to. *J. Fluid Mech.* **774**, 395–415.

Lozano-Durán, A.án & Bae, H.J. 2019 Characteristic scales of Townsend's wall-attached eddies. *J. Fluid Mech.* **868**, 698–725.

Lozano-Durán, A., Flores, O. & Jiménez, J. 2012 The three-dimensional structure of momentum transfer in turbulent channels. *J. Fluid Mech.* **694**, 100–130.

Marusic, I. & Monty, J.P. 2019 Attached eddy model of wall turbulence. *Annu. Rev. Fluid Mech.* **51**, 49–74.

Marusic, I., Monty, J.P., Hultmark, M. & Smits, A.J. 2013 On the logarithmic region in wall turbulence. *J. Fluid Mech.* **716**, R3.

McKeon, B.J. 2019 Self-similar hierarchies and attached eddies. *Phys. Rev. Fluids* **4** (8), 082601.

Nath, P. & Hickey, J.-P. 2026 Features of the attached-eddy hypothesis in one-dimensional turbulence models of turbulent boundary layers. *Phys. Rev. Fluids* **11** (1), 014604.

Nickels, T.B., Marusic, I., Hafez, S. & Chong, M.S. 2005 Evidence of the k_1^{-1} law in a high-Reynolds-number turbulent boundary layer. *Phys. Rev. Lett.* **95** (7), 074501.

Perry, A.E. & Chong, M.S. 1982 On the mechanism of wall turbulence. *J. Fluid Mech.* **119**, 173–217.

Perry, A.E. & Marušić, I. 1995 A wall-wake model for the turbulence structure of boundary layers. Part 1. Extension of the attached eddy hypothesis. *J. Fluid Mech.* **298**, 361–388.

Rice, S.O. 1944 Mathematical analysis of random noise. *Bell Syst. Tech. J.* **23** (3), 282–332.

https://doi.org/10.1017/jfm.2026.12182 Published online by Cambridge University Press

SAMIE, M., MARUSIC, I., HUTCHINS, N., FU, M.K., FAN, Y., HULTMARK, M. & SMITS, A.J. 2018 Fully resolved measurements of turbulent boundary layer flows up to. *J. Fluid Mech.* **851**, 391–415.

TOWNSEND, A.A.R. 1976 *The Structure of Turbulent Shear Flow*. Cambridge University Press.

WOODCOCK, J.D. & MARUSIC, I. 2015 The statistical behaviour of attached eddies. *Phys. Fluids* **27** (1), 015104.

YANG, X.I.A., MARUSIC, I. & MENEVEAU, C. 2016 Hierarchical random additive process and logarithmic scaling of generalized high order, two-point correlations in turbulent boundary layer flow. *Phys. Rev. Fluids* **1** (2), 024402.

https://doi.org/10.1017/jfm.2026.12182 Published online by Cambridge University Press